OPTICAL TECHNOLOGY FOR ARBITRARILY MANIPULATING AMPLITUDES AND PHASES OF HIGHLY DISCRETE SPECTRA

CHUAN ZHANG

THE UNIVERSITY OF ELECTRO-COMMUNICATIONS

TOKYO, JAPAN

January 2020

OPTICAL TECHNOLOGY FOR ARBITRARILY MANIPULATING AMPLITUDES AND PHASES OF HIGHLY DISCRETE SPECTRA

by

Chuan ZHANG

A thesis submitted in partial fulfillment of the requirements for the degree of Doctor of Philosophy

to

Department of Engineering Science
Graduate School of Informatics and Engineering
The University of Electro-Communications
Chofu, Tokyo, Japan
January 2020

Dedicated to my parents

Xiaomao ZHANG & Jufen JIA

"Physics has a history of synthesizing many phenomena into a few theories."

–Richard P. Feynman

Acknowledgements

I just can not believe how time has flied by! I would like to, hereby, grab the precious opportunity to acknowledge those who have helped me tremendously throughout my PhD career.

First and foremost, I would like to thank my supervisor, Prof. Masayuki Katsuragawa, for his thoughtful care and professional instructions all across my PhD life in UEC. It is his excellent research capability and generous dedication that lead to the accomplishment of my PhD degree.

I appreciate Prof. Kaoru Minoshima, and Prof. Masaru Suzuki for their patient instructions and helpful advices. I thank Yukai Furukawa sensei for his longtime assistance in whatever conducting experiments or analyzing theories.

I feel fairly grateful for Dr. Kazumi Yoshii and Dr. Chiaki Ohae on their constructive advices during my research work. I also acknowledge Dr. Jian Zheng, Dr. Nurul Sheeda Binti Suhaimi, and Dr. Trivikramarao Gavara for their selfless help in my PhD life. I, especially, appreciate Dmitry Trigubov for the period of time when we cooperated and moved forward together in the lab.

I would also like to thank all the other labmates who have literally contributed vastly to my happy life in the big family of Katsuragawa lab. Without them, it would be hardly probable for me to make good progress in any aspect. Special thanks also attributing to Weiyong Liu, Yoshisaki Kun, Morimune Kun, Suzuki Kun, Shikanai Kun, Watanabe Kun, et al.

Additionally, I have to thank all my nice friends in UEC, with whom I have promoted my communications, enriched my leisure time, and expanded my horizons. All these things during studying abroad will be memorable and nostalgic in my life afterwards.

Most importantly, I would like to say a big thank-you to my family for their nothing but great support and encouragement. My parents ever communicated with me many many times during the highs and lows of my PhD career.

Abstract

This thesis reports a novel optical technology that enables us to arbitrarily manipulate amplitudes and phases of highly discrete broadband spectra. The novel optical technology is concise: we simply place a few fundamental optical elements–a waveplate, a polarizer, and a transparent dispersive plate–on an optical axis and precisely control their thicknesses. However, such optical technology is practically useful: 1, excellent maintenance of beam quality and spatial coherence, as it can arbitrarily manipulate amplitudes and phases of any highly discrete (several tens of terahertz) spectrum without separating individual components in space; 2, resistance to high power lasers, as transparent materials with high damage thresholds are used for transmitting ultrabroad spectra (mid-infrared, visible, and ultraviolet).

We experimentally demonstrate the novel optical technology by manipulating amplitudes and phases of a series of vibrational Raman coherence, which has a frequency spacing of about 125 terahertz and a bandwidth of over 700 terahertz. Specifically, we have succeeded consecutively in manipulating the amplitudes and phases of five (spanning 2,403 to 481 nm), six (spanning 2,403 to 401 nm), and seven (spanning 2,403 to 343 nm) Raman components. Limited by the range of measuring phases of broader spectrum via spectral phase inteferometry, the current system can not handle eight or more Raman components.

As a typical application of such optical technology, we also demonstrate generation of ultrashort pulses in the time domain, through reconstructing electric field intensity waveforms of the Raman coherence after manipulating its amplitudes and phases. With the aforementioned five Raman components manipulated, we have achieved a train of 1.6 femtosecond (at full width at half maximum) pulses with a repetition rate of about 125 terahertz, close to Fourier transform limited condition. With six Raman components, we have achieved a train of 1.4 femtosecond ultrafast pulses. And finally with seven Raman components, we have achieved a train of 1.2 femtosecond ultrafast pulses.

Table of Contents

List of Figures

List of Tables

Chapter 1

Introduction

1.1 Literature overview and motivation

1.1.1 Literature overview

Development of new optical technology always paves the way for the essential evolution of optical science. A handful of typical examples can be enumerated as below (also refer to figure 1.1).

In the time domain, the advent of dielectric multilayer chirped mirrors [1–3] offered solutions for spectral broadband dispersion control [4, 5], and thus enabled practical solid state femtosecond lasers [6–8]. Benefiting from ultra-high temporal resolution, mode-locked [9–11] femtosecond lasers [12–14] have ever allowed researchers to probe fast-evolving phenomena, such as chemical reactions at the molecular level [15, 16], and further spawned femtochemistry [17] (for which Ahmed Zewail was awarded the Nobel Prize for Chemistry in 1999) and attosecond science [18–20].

In the frequency domain, the use of photonic crystal fiber (PCF) [21–23] for spectral bandwidth broadening permitted self-referencing method to measure carrier envelope offset (CEO) frequency, thus advanced optical frequency comb (OFC) [24, 25]. With the capability of measuring absolute optical fre-

quencies, OFC technology (for which John L. Hall and Theodor W. Hansch were awarded the Nobel Prize for Physics in 2005) has revolutionized optical frequency metrology [26] and precision spectroscopy [27].

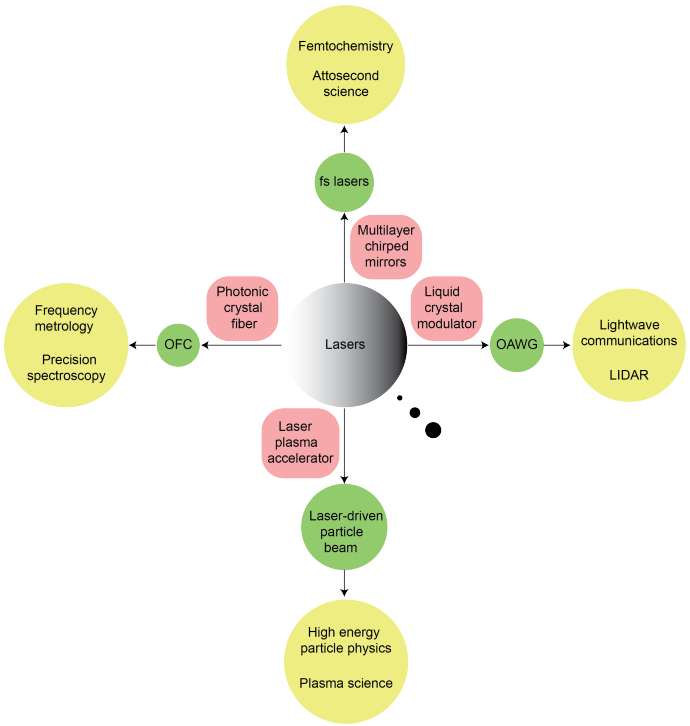

Figure 1.1: Key optical technologies open the doors for new optical sciences.

In addition, dominated by liquid crystal modulators (LCM) [28, 29], optical arbitrary waveform generation (OAWG) [30, 31] techniques (see figure 1.2) provided a means of controlling spectral intensities and phases of optical waves, and synthesizing arbitrary optical waveforms. Combining optical frequency comb with pulse shaping, OAWG technology has the advantages to be widely applied to lightwave communications [32], light detection and ranging (LIDAR) [31, 33], etc.

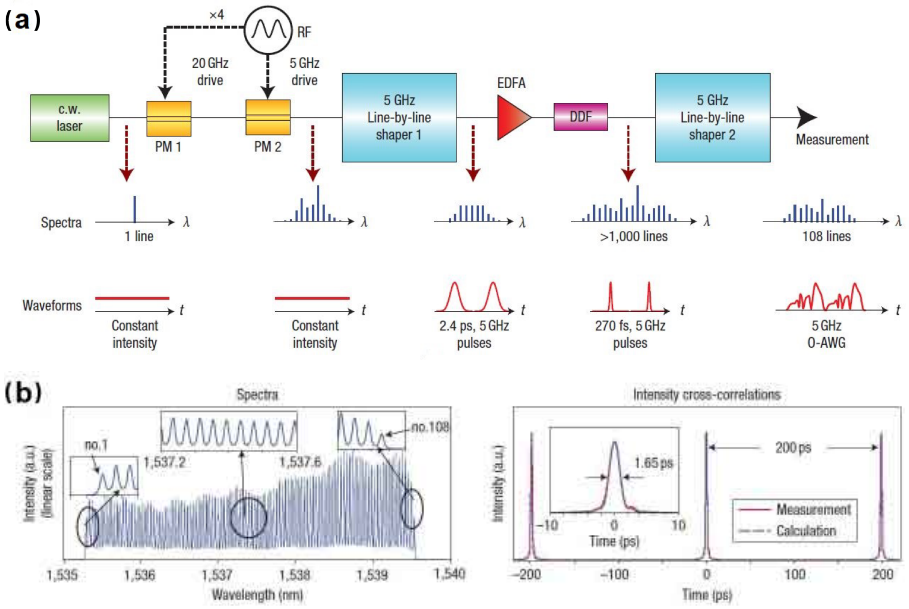

Figure 1.2: Experimental setup of OAWG techniques and the results of line-by-line shaping of 108 lines. (a), Schematic diagram. (b), Spectrum and intensity cross-correlation for the selected 108 lines at the exit. DDF: dispersion-decreasing fiber; RF: radio frequency; EDFA: erbium-doped fiber amplifier. [Courtesy of *Nature Photonics* ***1,*** *463 (2007).*] [34]

Although in an interdisciplinary way, by using high intensity lasers to interact with matters to produce a plasma ambience, such as protons and ions, the adoption of laser plasma accelerators enabled the acceleration of lighter particles such as electrons and positrons, thus making laser-driven particle beams [35]. With the unique characteristics of high energy and high quality, laser driven particle beams are expected to be useful in a wide range of contexts, including high energy particle physics, plasma science, medical treatment, etc.

1.1.2 The motivation of our work

Launched in the beginning of the 21st century, attosecond pulses [36–38] have been one of the most prominent frontiers in optical science [39–44], and have led the trend of exploring ever fast-evolving events [45–47] at an atomic scale.

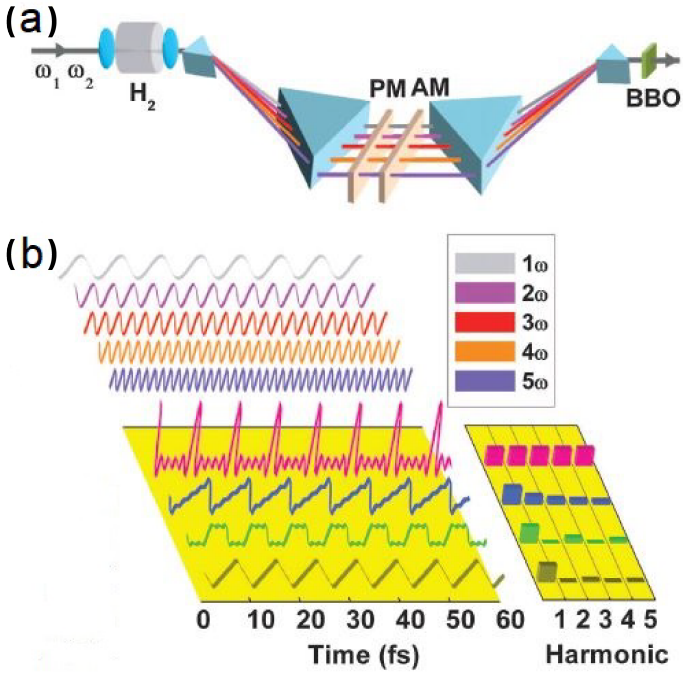

Figure 1.3: Schematic diagram of the field synthesis experiments conducted by Han S. Chan, et al. (a), Schematic diagram of the experimental setup to synthesize waveforms using harmonics generated by coherent modulation of the H_2 molecules. AM and PM are liquid crystal spatial light modulators (LC-SLMs) that, respectively, attenuate the powers (and thus amplitudes) of the harmonics, and adjust and compensate their phases; and these two abbreviations are only used here. These LCSLMs are also used as pulse shapers for the cross-correlation measurements. (b), Pictorial demonstration of ultrafast waveforms obtained by the coherent superposition of the first five harmonics of a fundamental wavelength. The panel on the lower right depicts the spectral field amplitudes required for the synthesis of the respective waveforms on the left. The 8.02-fs pulse spacing originates from a fundamental wavelength of 2,406 nm. [Courtesy of *Science* ***331,*** *1165 (2011).*] [48]

On the other hand, Stephen E. Harris and collaborators [49–52] provided a way of generating sub-femtosecond pulses via molecular modulation [53, 54] in the 1990s. A. H. Kung and others [48] experimentally verified to manipulate amplitudes and phases of five discrete Raman components and were able to synthesize arbitrary optical waveforms (see figure 1.3).

Motivated by the above backdrops, we expected to experimentally combine the techniques of synthesizing optical waveforms (pulse shaping in a broad sense), with a highly discrete Raman coherence (an optical frequency comb in a broad sense) to approach attosecond pulses in the time domain. Note that this discrete spectrum of Raman coherence is produced by molecular modulation process, not through high harmonic generation [55–57] that can yield ultrashort pulses with a pulse duration of several tens of attoseconds (scattering extreme ultra violet or soft X rays [58–60]),

In this thesis, I report a novel optical technology, which allows us to arbitrarily manipulate amplitudes and phases of highly discrete broadband spectra. The optical technology is simple, that is, we just place a few fundamental optical elements–a waveplate, a polarizer, and a transparent dispersive plate–on an optical axis and precisely control their thicknesses.

In spite of its simplicity, the novel optical technology is very powerful. Unlike line-by-line shapers [61, 62] used in OAWG techniques, we do not spatially separate the optical waves to control spectral components individually (such case can also be found in figure 1.3). Therefore, one of the attractive advantages is that the manipulation devices maintain excellent spatial coherence of the optical waves. Moreover, the manipulation devices are very robust to resist high energy laser radiations, as we exploit transparent materials that all have high damage thresholds.

We have, so far, applied our manipulation devices to harness the amplitudes and phases of five, six, and seven adiabatically driven vibrational Raman components (with a frequency spacing of about 125 THz) in sequence. With the broadest Raman spectrum–seven modes (covering 2,403 to 343 nm, with a bandwidth of over 700 terahertz)–handled, we have achieved a train of 1.2 femtosecond (at full width at half maximum) single-cycle pulses in the time domain, with a repetition period of about 8 femtoseconds.

In recent years, researchers have experimentally demonstrated optical field-induced changes in dielectric materials, namely, that the physical properties of dielectrics can be changed by controlling optical fields [63–65] on sub-femtosecond to few-femtosecond timescales. As a potential application regarding high speed

information processing, in terms of light-to-light, the trains of ultrafast pulses we achieved may become a key tool in this field. Considering that researches on ultrafast optics have been continuously flourishing, more applications are about to be discovered.

1.2 Thesis overview

As narrated partly in the abstract, this thesis accounts for the proposal, theoretical analysis, and experimental demonstration of a novel optical technology–arbitrary manipulation of amplitudes and phases of highly discrete spectra. Through Fourier transform of the manipulated spectra, we are also able to reconstruct electric field intensity waveforms, which are trains of ultrashort pulses in the time domain. Below shows detailed contents of each chapter.

Chapter 2 conceptually illustrates the idea of amplitude manipulation, and phase manipulation, respectively. In particular, this chapter shows why the novel optical technology is eligible for manipulating amplitudes and phases of multi-frequencies, and the advantages of such optical technology.

Chapter 3 introduces the entire experimental system, which mainly encompasses three parts: generation of Raman coherence, amplitude and phase manipulations, and phase measurement.

The first part of the system yields the laser source for use, i.e., a highly discrete broadband spectrum. Afterwards, the second part is the core content of the novel optical technology–amplitude and phase manipulations. Finally, the third part introduces phase measurement through spectral phase interferometry, which is the difficult point of the whole system since its precision and limitation substantially affect the viability and development of such novel optical technology.

Chapter 4 shows the main results experimentally obtained. In section 4.1, I will show the actual photos of Raman components generated. In section 4.2, I will show the results of amplitude manipulation in detail. And in section 4.3, I will show the results of phase manipulation. As we have manipulated

amplitudes and phases of different number of Raman components, I will exhibit the results sequentially, namely, begin with the results of five, then to six, and eventually to seven Raman modes. As a typical application of our manipulation devices, in section 4.4, I will also show reconstruction of electric field intensity waveforms of different number of Raman components, which are trains of ultrashort pulses in the time domain.

Chapter 5 concentrates on the main issues discussed during the process of manipulating amplitudes and phases of different number of Raman modes. Especially, I will explain the difficulties of increasing the number of Raman modes for both amplitude and phase manipulations, the precision estimated, the differences of pulses following the escalation of the number of Raman modes, the limitations of the current system, etc.

Chapter 6 summarizes the whole work in the thesis. Afterwards, this chapter gives prospects for future research, and examplifies potential applications of our novel optical technology, including its achievement of ultrashort pulses.

Bibliography of Chapter 1

[1] F. X. Kartner et al. “Design and fabrication of double-chirped mirrors”. In: *Opt. Lett.* 22 (1997), pp. 831–833.

[2] R. Szipocs and A. K. Kis. “Theory and design of chirped dielectric laser mirrors”. In: *Appl. Phys. B* 65 (1997), pp. 115–135.

[3] N. Matuschek, F. X. Kartner, and U. Keller. “Theory of double-chirped mirrors”. In: *IEEE J. of Selected Topics In Quant. Elect.* 4 (1998), pp. 197–208.

[4] R. Szipocs et al. “Chirped multilayer coatings for broadband dispersion control in femtosecond lasers”. In: *Opt. Lett.* 19 (1994), pp. 201–203.

[5] N. Matuschek et al. “Back-side-coated chirped mirrors with ultra-smooth broadband dispersion characteristics”. In: *Appl. Phys. B* 71 (2000), pp. 509–522.

[6] A. Stingl et al. “Sub-10-fs mirror-dispersion-controlled Ti:sapphire laser”. In: *Opt. Lett.* 20 (1995), pp. 602–604.

[7] E. J. Mayer et al. “Ultrabroadband chirped mirrors for femtosecond lasers”. In: *Opt. Lett.* 22 (1997), pp. 528–530.

[8] V. Pervak et al. “High-dispersive mirrors for femtosecond lasers”. In: *Opt. Express* 16 (2008), pp. 10220–10232.

[9] E. P. Ippen. “Principles of passive mode locking”. In: *Appl. Phys. B* 58 (1994), pp. 159–170.

[10] S. T. Cundiff, J. Ye, and J. L. Hall. “Optical frequency synthesis based on mode-locked lasers”. In: *Rev. of Sci. Inst.* 72 (2001), pp. 3749–3771.

[11] A. Bartels, D. Heinecke, and S. A. Diddams. “Passively mode-locked 10 GHz femtosecond Ti:sapphire laser”. In: *Opt. Lett.* 33 (2008), pp. 1905–1907.

[12] U. Morgner et al. “Sub-two-cycle pulses from a Kerr-lens mode-locked Ti:sapphire laser”. In: *Opt. Lett.* 24 (1999), pp. 920–922.

[13] L. Gallmann et al. “Characterization of sub-6-fs optical pulses with spectral phase interferometry for direct electric-field reconstruction”. In: *Opt. Lett.* 24 (1999), pp. 1314–1316.

[14] M. Miranda et al. “Simultaneous compression and characterization of ultrashort laser pulses using chirped mirrors and glass wedges”. In: *Opt. Express* 20 (2012), pp. 688–697.

[15] M. Shapiro and P. Brumer. “Coherent control of molecular dynamics”. In: *Rep. Prog. Phys.* 66 (2003), pp. 859–942.

[16] C. Brif, R. Chakrabarti, and H. Rabitz. “Control of quantum phenomena: Past, present and future”. In: *New J. Phys.* 12 (2010), p. 075008.

[17] A. H. Zewail. “Femtochemistry: atomic-scale dynamics of the chemical bond”. In: *J. Phys. Chem. A* 104 (2000), pp. 5660–5694.

[18] M. Hentschel et al. “Attosecond metrology”. In: *Nature* 414 (2001), pp. 509–513.

[19] P. B. Corkum and F. Krausz. “Attosecond science”. In: *Nat. Phys.* 3 (2007), pp. 381–387.

[20] F. Krausz and M. K. Stockman. “Attosecond metrology: from electron capture to future signal processing”. In: *Nat. Photon.* 8 (2014), pp. 205–213.

[21] J. C. Knight et al. “All-silica single-mode optical fiber with photonic crystal cladding”. In: *Opt. Lett.* 21 (1996), pp. 1547–1549.

[22] T. A. Birks, J. C. Knight, and P. S. J. Russell. “Endlessly single-mode photonic crystal fiber”. In: *Opt. Lett.* 22 (1997), pp. 961–964.

[23] J. C. Knight. “Photonic crystal fibers”. In: *Nature* 424 (2003), pp. 847–851.

[24] T. Udem et al. “Absolute optical frequency measurement of the cesium D1 line with a mode-locked laser”. In: *Phys. Rev. Lett.* 82 (1999), pp. 3568–3571.

[25] D. J. Jones et al. “Carrier-envelope phase control of femtosecond mode-locked lasers and direct optical frequency synthesis”. In: *Science* 288 (2000), pp. 635–639.

[26] T. Udem, R. Holzwarth, and T. W. Hansch. “Optical frequency metrology”. In: *Nature* 416 (2002), pp. 233–237.

[27] R. Holzwarth et al. “Optical frequency synthesizer for precision spectroscopy”. In: *Phys. Rev. Lett.* 85 (2000), pp. 2264–2267.

[28] A. M. Weiner et al. “Programmable shaping of femtosecond pulses by use of a 128-element liquid-crystal phase modulator”. In: *IEEE J. Quant. Electron.* 28 (1992), pp. 908–920.

[29] M. M. Wefers and K. A. Nelson. “Generation of high-fidelity programmable ultrafast optical waveforms”. In: *Opt. Lett.* 20 (1995), pp. 1047–1049.

[30] Z. Jiang, D. E. Leaird, and A. M. Weiner. “Line-by-line pulse shaping control for optical arbitrary waveform generation”. In: *Opt. Express* 13 (2005), pp. 10431–10439.

[31] A. M. Weiner. “Ultrafast optical pulse shaping: a tutorial review”. In: *Opt. Comm.* 284 (2011), pp. 3669–3692.

[32] D. J. Geisler et al. “Modulation-format agile, reconfigurable Tb/s transmitter based on optical arbitrary waveform generation”. In: *Opt. Express* 17 (2009), pp. 15911–15925.

[33] S. T. Cundiff and A. M. Weiner. “Optical arbitrary waveform generation”. In: *Nat. Photon.* 4 (2010), pp. 760–766.

[34] Z. Jiang et al. “Optical arbitrary waveform processing of more than 100 spectral comb lines”. In: *Nat. Photon.* 1 (2007), pp. 463–467.

[35] v. Malka et al. “Principles and applications of compact laser–plasma accelerators”. In: *Nat. Phys.* 4 (2008), pp. 447–453.

[36] J. Itatani et al. “Attosecond streak camera”. In: *Phys. Rev. Lett.* 88 (2002), p. 173903.

[37] M. Kitzler et al. “Quantum theory of attosecond XUV pulse measurement by laser dressed photoionization”. In: *Phys. Rev. Lett.* 88 (2002), p. 173904.

[38] E. Goulielmakis et al. “Attosecond control and measurement: lightwave electronics”. In: *Science* 317 (2007), pp. 769–775.

[39] A. L. Schawlow and C. H. Townes. “Infrared and optical masers”. In: *Phys. Rev.* 112 (1958), pp. 1940–1949.

[40] T. H. Maiman. “Stimulated optical radiation in ruby”. In: *Nature* 187 (1960), pp. 493–494.

[41] P. A. Franken et al. “Generation of optical harmonics”. In: *Phys. Rev. Lett.* 7 (1961), pp. 118–119.

[42] J. A. Armstrong et al. “Interactions between light waves in a nonlinear dielectric”. In: *Phys. Rev.* 127 (1962), pp. 1918–1939.

[43] R. L. Fork et al. “Compression of optical pulses to six femtoseconds by using cubic phase compensation”. In: *Opt. Lett.* 12 (1987), pp. 483–485.

[44] J. C. Diels and W. Rudolph. “Compression of high-power optical pulses”. In: *J. Opt. Soc. Am. B* 5 (1988), pp. 641–647.

[45] T. L. Cocker et al. “Tracking the ultrafast motion of a single molecule by femtosecond orbital imaging”. In: *Nature* 539 (2016), pp. 263–267.

[46] A. Baltuska et al. “Attosecond control of electronic processes by intense light fields”. In: *Nature* 421 (2003), pp. 611–615.

[47] A. Sommer et al. “Attosecond nonlinear polarization and light–matter energy transfer in solids”. In: *Nature* 534 (2016), pp. 86–90.

[48] H. S. Chan and others. “Synthesis and measurement of ultrafast waveforms from five discrete optical harmonics”. In: *Science* 331 (2011), pp. 1165–1168.

[49] S. E. Harris and A. V. Sokolov. “Subfemtosecond pulse generation by molecular modulation”. In: *Phys. Rev. Lett.* 81 (1998), pp. 2894–2897.

[50] A. V. Sokolov, D. D. Yavuz, and S. E. Harris. “Subfemtosecond pulse generation by rotational molecular modulation”. In: *Opt. Lett.* 24 (1999), pp. 557–559.

[51] A. V. Sokolov et al. “Generation and control of femtosecond pulses by molecular modulation”. In: *J. of Mod. Opt.* 52 (2005), pp. 285–304.

[52] M. Y. Shverdin et al. “Generation of a single-cycle optical pulse”. In: *Phys. Rev. Lett.* 94 (2005), p. 033904.

[53] N. Zhavoronkov and G. Korn. “Generation of single intense short optical pulses by ultrafast molecular phase modulation”. In: *Phys. Rev. Lett.* 88 (2002), p. 203901.

[54] S. Baker et al. “Femtosecond to attosecond light pulses from a molecular modulator”. In: *Nat. Photon.* 5 (2011), pp. 664–671.

[55] J. J. Macklin, J. D. Kmetec, and C. L. III Gordon. “High-order harmonic generation using intense femtosecond pulses”. In: *Phys. Rev. Lett.* 70 (1993), pp. 766–769.

[56] A. L’Huillier and P. Balcou. “High-order harmonic generation in rare gases with a 1-ps 1053-nm laser”. In: *Phys. Rev. Lett.* 70 (1993), pp. 774–777.

[57] C. Altucci et al. “Influence of atomic density in high-order harmonic generation”. In: *J. Opt. Soc. Am. B* 13 (1996), pp. 148–156.

[58] P. Saliéres et al. “Frequency-domain interferometry in the XUV with high-order harmonics”. In: *Phys. Rev. Lett.* 83 (1999), pp. 5483–5486.

[59] Y. Mairesse et al. “Attosecond synchronization of high-harmonic soft x-rays”. In: *Science* 302 (2003), pp. 1540–1543.

[60] N. Dudovich et al. “Measuring and controlling the birth of attosecond XUV pulses”. In: *Nat. Phys.* 2 (2006), pp. 781–786.

[61] K. R. Pandiri et al. “Line-by-line control of 10-THz-frequency-spacing Raman sidebands”. In: *Opt. Express* 18 (2010), pp. 732–739.

[62] K. R. Pandiri and M. Katsuragawa. “A 10 THz ultrafast function generator-generation of rectangular and triangular pulse trains”. In: *New J. Phys.* 13 (2011), p. 023030.

[63] A. Schiffrin et al. “Optical- field-induced current in dielectrics”. In: *Science* 493 (2013), pp. 70–74.

[64] M. Schultze et al. “Controlling dielectrics with the electric field of light”. In: *Nature* 493 (2013), pp. 75–78.

[65] T. Rybka et al. “Sub-cycle optical phase control of nanotunnelling in the single-electron regime”. In: *Nat. Photon.* 10 (2016), pp. 667–670.

Chapter 2

Conceptual idea of the novel optical technology

In this chapter, I will illustrate conceptual idea of the novel optical technology– amplitude and phase manipulations.

The idea of the novel optical technology is very realistic: we have already been able to control an optical wave with a single frequency flexibly, whether in terms of its amplitude, or phase. In detail, we can exploit an anisotropic material (waveplate in a broad sense) and a polarizer to control the polarization direction and intensity (thus amplitude) of output laser (i.e., manipulation of amplitude, MA); and utilize a transparent dispersive plate to control the phase of transmitted laser (i.e., manipulation of phase, MP). These are basic optical principles. However, what if the incident optical wave has a broad spectrum with several discrete frequencies, especially, some peculiar spectrum resembling vibrational Raman coherence (with a large frequency spacing)? Can we still arbitrarily manipulate amplitudes and phases of such broad spectrum? The answer to this question is affirmative. That is, we can imitate the case of controlling amplitude and phase of a monochromatic laser, to control amplitudes and phases of a broad discrete spectrum with a large frequency spacing.

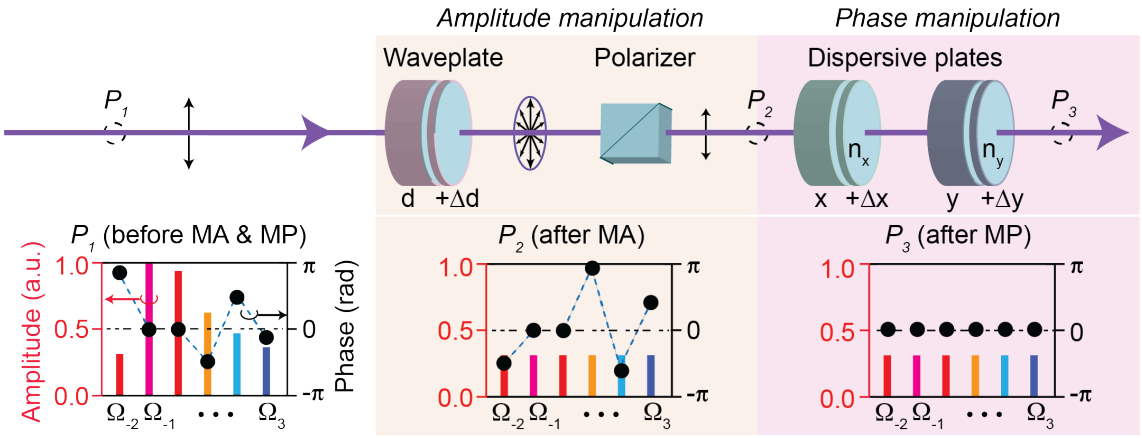

Figure 2.1: Conceptual idea of manipulating amplitudes and phases of multiple components. Without loss of generality, we put the number of spectral components to six. Note that the diagram shows a top view of such idea. P_1, P_2, and P_3 correspond to different positions on the optical axis, which are before manipulating amplitudes (MA), after MA, and after manipulating phases (MP), respectively. Bidirectional-black arrows and the ellipse behind the waveplate represent polarization states at respective positions; $d + \Delta d$, $x + \Delta x$, and $y + \Delta y$ are adjustable thicknesses of different plates; n_x and n_y are refractive indices of the two dispersive plates; Ω_{-2}–Ω_3 are frequencies of different components.

Figure 2.1 shows the conceptual idea of arbitrary manipulation on amplitudes and phases. The middle part (light yellow background) depicts compact setup for MA, and the rightmost part (pink background) depicts setup for MP. See the next two sections for details.

Afterwards, I will show the principle of SPIDER system, which was used for measuring phases of highly discrete spectra.

These three sections make up core contents of theory of the novel optical technology.

2.1 Conceptual idea of amplitude manipulation

The physical mechanism of our amplitude manipulation is by using birefringent property in anisotropic materials. According to the principle of optical birefringence in an anisotropic material [66], the phase retardation between ordinary and extraordinary rays is given by

$$\Gamma_m = \frac{2\pi\Omega_m}{c}(n_{m,e} - n_{m,o})\Delta d \tag{2.1}$$

where subscript m= -2, -1, ..., indicates mode number of the spectrum; Ω_m, $n_{m,e}$ and $n_{m,o}$ are frequency, refractive indices of the extraordinary, and ordinary rays in the waveplate, respectively; c is the speed of light in vacuum; and Δd is thickness change of the waveplate.

To put simply, in experiment, we set the optical axis of the waveplate 45 degrees to the direction of linear polarization of the incident laser. Taking into account decreasing reflection loss at surfaces of MA and MP elements, we set both the direction of linear polarization of the incident laser and the transmission direction of the polarizer to be *p*-polarized (refer to figure 2.1). With the above settings, laser intensity after transmitting through the polarizer is given as

$$I_m = \cos^2(\frac{\Gamma_m}{2}) \tag{2.2}$$

or

$$I_m = \cos^2(\frac{\pi\Omega_m}{c}(n_{m,e} - n_{m,o})\Delta d) \tag{2.3}$$

which is a sinusoidal function of the thickness change of the waveplate, Δd, and hence periodical. By varying thickness of the waveplate, we can observe periodical oscillations of intensities at the exit.

What is noteworthy is that the spectrum to be handled should be highly discrete–frequency spacing ($\Delta\Omega = \Omega_{m+1} - \Omega_m$) is of several tens of terahertz–

so that Ω_m (and thus Γ_m) differs drastically depending on its mode number, m. In other words, output intensities of various modes oscillate distinctively, in terms of their periods as a function of the thickness of the waveplate. As a result, this makes it feasible to arbitrarily manipulate intensities (or amplitudes) of multiple frequencies simultaneously.

Given that the above concept concerns changing the thickness of the waveplate to realize intensity oscillations, adjustment of the thickness of the waveplate (actually, both the anisotropic crystal and the transparent dispersive plate) should reach a fine resolution (5 μm) over a wide range (at least 10 mm estimated). Therefore, how we can precisely and handily harness thickness change of the waveplate becomes one of the key points in practical experiment. This issue will be mentioned again and get tackled in the part of experimental system in chapter 3.

Another key point in experiment is that since we expect to manipulate several amplitudes at the same time, oscillations of different components, considered altogether, are very complicated and even random to some extent. It is hardly possible for us to directly predict or determine an optimal solution, which may be extremely large and unrealistic. Nevertheless, as key physics discovered [67]: when the discreteness (i.e., frequency spacing) of optical spectrum is high enough (to the order of a few tens of terahertz), we abandon the insistence of exactly finding an analytic solution, but try to find approximate solutions, which frequently appear with sufficient accuracy (more practical in such sense), through numerical exploration. In other words, we will numerically explore an optimal thickness close to the ideal solution (analytic) for manipulating amplitudes (same as the case of manipulating phases), and then validate it in real experiment.

Generally, the more complicated the amplitude distribution we want to achieve is, the more difficult it is to find an optimal thickness through numerical exploration. If we want to arbitrarily manipulate amplitudes to any complicated distribution, we should have very wide range of thickness change of crystal quartz for numerical exploration, which is unrealistic. However, since we would like to achieve ultrashort pulses in the time domain, we need to tailor amplitudes of the spectrum to a 'flat' distribution, which makes sense that it is a proof of

our novel optical technology in reality.

Based on the idea of numerical exploration, we desire to manipulate multiple intensities at exit of the waveplate. As shown in figure 2.1, before manipulating (inset-P_1), intensities of various components may be greatly different. However, using the novel optical technology, ideally we are able to flatten all the intensities/ amplitudes to the same value (inset-P_2), which contributes to generating a train of ultrafast pulses.

2.2 Conceptual idea of phase manipulation

The physical mechanism of our phase manipulation is by using chromatic dispersion in transparent materials. Based on the principle of chromatic dispersion, we have to take into account high order dispersions of a broadband spectrum [68] in dispersive materials.

$$\phi(\Omega_m) = \sum_{k=0}^{m-1} (\Phi_k \Delta L (m\Delta\Omega)^k) \tag{2.4}$$

where *m* represents different spectral components; $\phi(\Omega_m)$ is spectral phase to be determined; Φ_k is coefficient of the *k*-th order dispersion with respect to $\phi(\Omega_m)$; ΔL is thickness change of the transparent material.

Given a spectrum with *m* components, the phase, $\phi(\Omega_m)$ should be expanded up to the *k=(m-1)*-st order dispersion. In other words, to determine a spectrum with *m* components, we need to consider its dispersions from the zeroth order up to the *(m-1)*-st order.

It is noteworthy that the physical mechanism of phase manipulation is similar to that of amplitude manipulation: depending on component of the highly discrete spectrum, different order dispersion, $\Phi_k \Delta L (m\Delta\Omega)^k$ has largely different coefficient, $\Phi_k (m\Delta\Omega)^k$. For example, taking into account fused silica, coefficients are: $\Phi_2(\Delta\Omega)^2$ = - 1.786 $\times 10^2$ rad/mm, $\Phi_3(\Delta\Omega)^3$ = 6.664 $\times 10^0$ rad/mm, and , $\Phi_4(\Delta\Omega)^4$ = - 4.602 $\times 10^{-1}$ rad/mm. Such conditions can also be found for the

case of calcium fluoride. By varying thickness of the transparent dispersive material, ΔL, we are able to alter each spectral phase $\phi(\Omega_m)$ independently and arbitrarily.

Generally, to determine spectral phases exactly in a dispersive material, we have to solve the set of equations as below.

$$\phi(\Omega_m) = \sum_{k=0}^{m-1}(\Phi_k \Delta L(m\Delta\Omega)^k) = p_m + 2q_m\pi \tag{2.5}$$

where $0 \leq p_m < 2\pi$; q_m is an integer.

As a typical example, if we assume that there are five components, i.e., m = 5, equation 2.5 can be given as:

$$\phi(\Omega_m) = \sum_{k=0}^{4}(\Phi_k \Delta L(m\Delta\Omega)^k) = p_m + 2q_m\pi \tag{2.6}$$

Refer to [68]. To simplify notations, we let $\Phi_k \Delta L = \Psi_k$. Thus, the above equation can be transformed as:

$$\phi(\Omega_1) = \Psi_0 + \Psi_1(\Delta\Omega) + \Psi_2(\Delta\Omega)^2 + \Psi_3(\Delta\Omega)^3 + \Psi_4(\Delta\Omega)^4 = p_1 + 2q_1\pi$$

$$\phi(\Omega_2) = \Psi_0 + \Psi_1(2\Delta\Omega) + \Psi_2(2\Delta\Omega)^2 + \Psi_3(2\Delta\Omega)^3 + \Psi_4(2\Delta\Omega)^4 = p_2 + 2q_2\pi$$

$$\phi(\Omega_3) = \Psi_0 + \Psi_1(3\Delta\Omega) + \Psi_2(3\Delta\Omega)^2 + \Psi_3(3\Delta\Omega)^3 + \Psi_4(3\Delta\Omega)^4 = p_3 + 2q_3\pi$$

$$\phi(\Omega_4) = \Psi_0 + \Psi_1(4\Delta\Omega) + \Psi_2(4\Delta\Omega)^2 + \Psi_3(4\Delta\Omega)^3 + \Psi_4(4\Delta\Omega)^4 = p_4 + 2q_4\pi$$

$$\phi(\Omega_5) = \Psi_0 + \Psi_1(5\Delta\Omega) + \Psi_2(5\Delta\Omega)^2 + \Psi_3(5\Delta\Omega)^3 + \Psi_4(5\Delta\Omega)^4 = p_5 + 2q_5\pi \tag{2.7}$$

Using the techniques of matrix, we can obtain solutions as below:

$$\Psi_0 = 5(p_1 + 2q_1\pi) - 10(p_2 + 2q_2\pi) + 10(p_3 + 2q_3\pi) - 5(p_4 + 2q_4\pi) + (p_5 + 2q_5\pi)$$

$$\Psi_1 = \frac{1}{12\Delta\Omega}(-77(p_1 + q_1\pi) + 214(p_2 + q_2\pi) - 234(p_3 + 2q_3\pi) + 122(p_4 + 2q_4\pi) - 25(p_5 + 2q_5\pi))$$

$$\Psi_2 = \frac{1}{24\Delta\Omega^2}(71(p_1 + q_1\pi) - 236(p_2 + q_2\pi) + 294(p_3 + 2q_3\pi) - 164(p_4 + 2q_4\pi) + 35(p_5 + 2q_5\pi))$$

$$\Psi_3 = \frac{1}{12\Delta\Omega^3}(-7(p_1+q_1\pi)+26(p_2+q_2\pi)-36(p_3+2q_3\pi)+22(p_4+2q_4\pi)-5(p_5+2q_5\pi))$$

$$\Psi_4 = \frac{1}{24\Delta\Omega^4}((p_1 + q_1\pi) - 4(p_2 + q_2\pi) + 6(p_3 + 2q_3\pi) - 4(p_4 + 2q_4\pi) + (p_5 + 2q_5\pi)) \quad (2.8)$$

However, since this thesis mainly concerns with generating ultrashort pulses, the zeroth order dispersion, Ψ_0, and the first order dispersion, Ψ_1, make no contribution to the shape of electric field intensity waveforms (to put it simply, the appearance of pulses), but only change the position (zeroth order) and the linear slope (first order) of intensity waveforms. As a consequence, we can neglect dispersions of the zeroth and first orders.

To further simplify the notation, we make $\phi_k = \Psi_k(\Delta\Omega)^k$. Therefore, equation 2.8 can be given as:

$$\begin{aligned}\phi_2 = \frac{1}{24}&(71(p_1+q_1\pi)-236(p_2+q_2\pi)+294(p_3+2q_3\pi)-164(p_4+2q_4\pi)+35(p_5+2q_5\pi))\\ &= \frac{1}{24}(2\pi(71q_1 - 2^2\times59q_2 + 2\times3\times7^2q_3 - 2^2\times41q_4 + 5\times7q_5)\\ &\quad + (71p_1 - 2^2\times59p_2 + 2\times3\times7^2p_3 - 2^2\times41p_4 + 5\times7p_5))\\ &= \frac{1}{24}(2\pi A + B)\end{aligned} \quad (2.9)$$

where

$$A = 71q_1 - 2^2{\times}59q_2 + 2{\times}3{\times}7^2q_3 - 2^2{\times}41q_4 + 5{\times}7q_5 \tag{2.10}$$

$$B = 71p_1 - 2^2{\times}59p_2 + 2{\times}3{\times}7^2p_3 - 2^2{\times}41p_4 + 5{\times}7p_5 \tag{2.11}$$

Similarly, we can obtain:

$$\begin{aligned}\phi_3 = \frac{1}{12}(2\pi(-7q_1 + 26q_2 - 36q_3 + 22q_4 - 5q_5) + (-7p_1 + 26p_2 - 36p_3 + 22p_4 - 5p_5)) \\ = \frac{1}{24}(2\pi C + D)\end{aligned} \tag{2.12}$$

where

$$C = -7q_1 + 26q_2 - 36q_3 + 22q_4 - 5q_5 \tag{2.13}$$

$$D = -7p_1 + 26p_2 - 36p_3 + 22p_4 - 5p_5 \tag{2.14}$$

And

$$\begin{aligned}\phi_4 = \frac{1}{24}(2\pi(q_1 - 4q_2 + 6q_3 - 4q_4 + q_5) + (p_1 - 4p_2 + 6p_3 - 4p_4 + p_5)) \\ = \frac{1}{24}(2\pi E + F)\end{aligned} \tag{2.15}$$

where

$$E = q_1 - 4q_2 + 6q_3 - 4q_4 + q_5 \tag{2.16}$$

$$F = p_1 - 4p_2 + 6p_3 - 4p_4 + p_5 \tag{2.17}$$

Since q_m is an integer, the term A (or C, E) is also an integer. Therefore, equation 2.9, 2.12, and 2.15 can be changed to:

$$\phi_2 = 2\pi\frac{Q_2}{24} + \frac{P_2}{24} \tag{2.18}$$

$$\phi_3 = 2\pi\frac{Q_3}{12} + \frac{P_3}{12} \tag{2.19}$$

$$\phi_4 = 2\pi\frac{Q_4}{24} + \frac{P_4}{24} \tag{2.20}$$

where Q_2 = 0, 1, ..., 23; Q_3 = 0, 1, ..., 11; Q_4 = 0, 1, ..., 23; P_2, P_3, and P_4 are real numbers determined by spectral phases p_m. Here, we obtain 24 values of ϕ_2, 12 values of ϕ_3, and 24 values of ϕ_4.

However, as the relations below exist:

$$A + C = 2(2^5 q_1 - 3 \times 5 \times 7 q_2 + 3 \times 43 q_3 - 71 q_4 + 3 \times 5 q_5) \tag{2.21}$$

$$A + E = 12(2^3 q_1 - 2^2 \times 5 q_2 + 5^2 q_3 - 2 \times 7 q_4 + 3 q_5) \tag{2.22}$$

$$C + E = 2(-3 q_1 + 11 q_2 - 15 q_3 + 9 q_4 - 2 q_5) \tag{2.23}$$

In detail, the sum of A and C is an even integer–Q_2 and Q_3 are both even or odd integers–making (24×12)/2 = 144 solutions in the solution space of (ϕ_2, ϕ_3). Similarly, the sum of A and E is an multiple of 12, making (24×24)/12 = 48 solutions in the solution space of (ϕ_2, ϕ_4). The sum of C and E is an even integer, also making (24×12)/2 = 144 solutions in the solution space of (ϕ_3, ϕ_4). Thereby, there are (24×12×24)/(2×12) = 288 solutions in total in the three dimensional solution space, (ϕ_2, ϕ_3, ϕ_4). These many exact solutions make it easy for us to find near-optimal solutions when manipulating spectral phases of multiple components. The numerous solutions to equation 2.5 features periodical behavior of spectral phase (with a period of 2π).

One might think of the method of integer temporal Talbot (ITT) (analytic, refer to [69–71], which requires a few dispersive materials (the number equals

to the order number of dispersions) with exact thicknesses to solve equation 2.5. Nevertheless, in reality, it is difficult to realize ITT method by using a number of dispersive materials with exact thicknesses, which may be very large, or even incredible scales. Hence, ITT method is conceptually different from our novel idea of phase manipulation.

Similar to the case of MA, in stead of finding exact solutions of equation 2.5 (analytic), we turn to numerically exploring approximate solutions close to Fourier transform limited (TL) condition. Generally, for an analytic solution, a few different kinds of dispersive materials with huge thicknesses are needed to exactly compensate high order dispersions, which is practically difficult. However, in numerical exploration, as long as all phases Ψ_m can approach zero radians closely after random inserting some thickness of transparent dispersive material, we are able to reconstruct ultrafast pulses near TL condition. As found unexpectedly (refer to [67, 68]), through sweeping thickness of a dispersive plate, we are able to frequently make all phases close to zero rad. This idea is practically useful and attractive in experiment. The approximate solutions appearing "repeatedly" are due to phase cycling of 2π, and this later makes quasi-periodical behaviors of peak intensities as functions of thicknesses of dispersive materials and contributes to the mechanism of improved precision in phase manipulation.

In numerical exploration, we assume that initial phases of the spectrum are Φ_m. After transmitting through the transparent plate, the phases are given as

$$\psi(\Omega_m) = \phi(\Omega_m) + 2\pi\frac{\Omega_m}{c}(\Delta L n_m) \tag{2.24}$$

Benefiting from the large frequency spacing, $\Delta\Omega$ of the spectrum, the frequency-dependent phases, $\psi(\Omega_m)$ vary differently with respect to the thickness of dispersive material, ΔL. In other words, by changing the thickness of dispersive plate, ΔL, we are able to acquire phase oscillations of different spectral components.

Now that the issue of phase manipulation turns to sweeping the thickness of

dispersive plate to numerically explore an optimum near TL condition. Therefore, the precision and resolution of adjustment of plate thickness are very crucial. Relevant designs will be introduced in chapter 3.

For the purpose of increasing flexibility of manipulating phases, we exploit two different kinds of dispersive materials that can independently control spectral phases. As a result, $\Delta L n_m \rightarrow (\Delta x n_{m,x} + \Delta y n_{m,y})$, where Δx, Δy and $n_{m,x}$, $n_{m,y}$ are thickness and refractive indices of two dispersive materials. Thus the equation of phase manipulation via numerical exploration becomes

$$\psi(\Omega_m) = \phi(\Omega_m) + 2\pi \frac{\Omega_m}{c}(\Delta x n_{m,x} + \Delta y n_{m,y}) \tag{2.25}$$

As shown in figure 2.1, we assume that the phases before manipulation (inset-P_2) may distribute messily with different values. However, after manipulating phases (MP), all phases (see inset-P_3) are ideally suppressed to zero rad (close to zero rad in practical experiment). This later will be set as our target in MP, in order to achieve ultrafast pulses.

2.3 Principle of SPIDER system

After manipulating phases, we still need to find a practical way to measure spectral phases. There are technically a handful of methods for measuring duration of ultrashort pulses, such as auto-correlation, frequency resolved optical grating (FROG) [72, 73], spectral phase interferometry for direct electric-field reconstruction (SPIDER) [74, 75], etc. However, as for measuring pulse duration together with spectral phases, the most predominant way usually comes to either FROG or SPIDER system. Despite that FROG system is also available for our purpose and has its own advantages in practice, it actually requires sophisticated iterative algorithm for phase retrieval, and thus takes much more time in experiment. Therefore, we use SPIDER system for phase measurement, which is slightly modified to be applicable for discrete spectra.

After propagating into the SPIDER system, Raman components (RCs) are

split into two arms by a window (uncoated ultraviolet fused silica): major portions (about 90%) of total energy are reflected as Raman components, and the rest are transmitted as reference components. Refer to figure 2.3 in chapter 2. After passing through long-pass filters (and SB-10 mirrors – for cutting off 2,403 nm), the arm of reference preserves only Ω_{-1} and Ω_0, i.e., 1,202 nm and 801 nm.

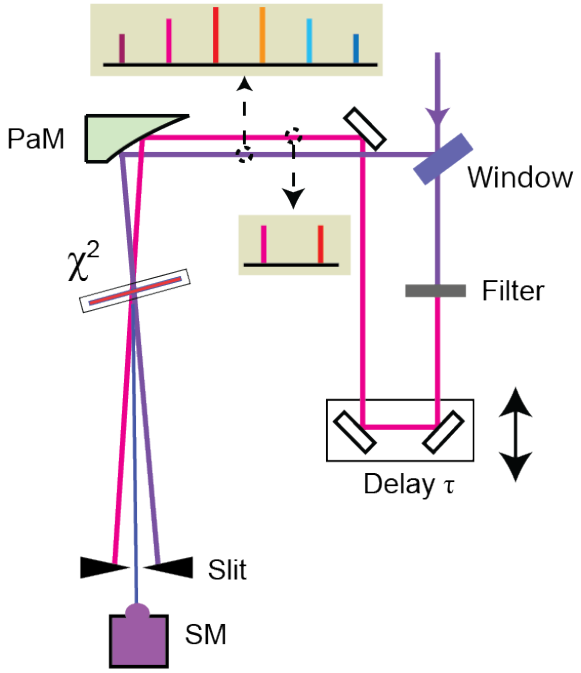

Figure 2.2: Schematic diagram of SPIDER system. Bidirectional-arrow denotes translation directions of delay stage; PaM, parabolic mirror; χ^2, nonlinear optical crystal; SM, spectrometer.

Figure 2.3 shows details of interfering process. As a typical example, we hereby show the case where the spectrum has six components (refer to chapter 4). At the nonlinear optical crystal, the two arms mix with each other and produce two replicas of the original spectrum. As shown in figure 2.3(a), frequencies of two replicas are actually shifted by $2\Delta\Omega$ (by taking a sum with Ω_{-1}) and $3\Delta\Omega$ (by taking a sum with Ω_0). Then two replicas interfere with each other, making overlapped frequencies serve as five SFG components (refer to 2.3(b)). Here, the five SFG components are phase correlated with the original spectrum.

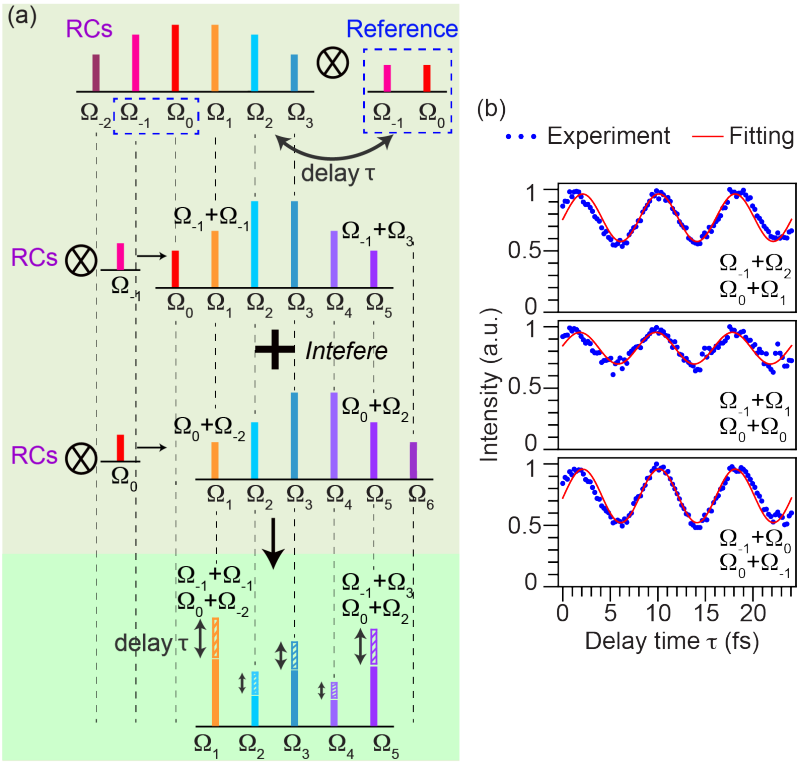

Figure 2.3: Mechanism of retrieving phases of a spectrum with six components in SPIDER system. (a), The process of interfering. (b), Typical examples of intensity oscillations of interfered signals obtained by spectrometer. RCs, Raman components.

With delay time τ existing in the reference arm, electric-field intensities of SFG components are given as

$$\begin{aligned} I_m^{SFG} &= |E_{m+1}E_{-1}^R e^{i\Omega_{-1}\tau} + E_m E_0^R e^{i\Omega_0\tau}|^2 \\ &= |E_{m+1}E_{-1}^R|^2 + |E_m E_0^R|^2 \\ &+ 2|E_{m+1}E_{-1}^R E_m E_0^R|\cos((\psi_{m+1}-\psi_m)+(\psi_{-1}^R-\psi_0^R)-\Delta\Omega\tau) \end{aligned} \tag{2.26}$$

where variables with superscript R represent the reference arm. Apparently, intensity oscillations of interfered SFG components are sinusoidal functions of delay time τ, and the period of each oscillation is fixed at $1/\Delta\Omega$ = 8.02 fs.

Diagrams of figure 2.3(b) indicate typical examples of intensity oscillations

of SFG components, with three different frequencies, Ω_2, Ω_3, and Ω_4, respectively. By fitting intensity oscillations with sine functions, we can retrieve spectral phases of SFG components. Certainly, here we need to take into account precision of fitting, which affects reliability of phase measurement via SPIDER system. Refer to relevant discussions in chapter 5. Hereafter, according to interfering process in equation 2.26, we are able to extract fundamental phases (i.e., phases of the original spectrum). Refer to [76] for more details.

Equiped with numerical exploration for phase manipulation and SPIDER system for phase measurement, we are able to thoroughly harness phases of a broad spectrum, and achieve ultrafast pulses near TL condition. After manipulating amplitudes and phases of a spectrum, we can use the following equation to reconstruct normalized electric field intensity waveforms in the time domain.

$$I_{pulse} = |\sum_{k=-2}^{m} E_k * \exp[i(2\pi\Omega_k t + \psi_k)]|^2 / (\sum_{k=-2}^{m} E_k)^2 \tag{2.27}$$

Bibliography of Chapter 2

[66] A. Yariv and P. Yeh. *Photonics: optical electronics in modern communications*. the sixth edition. Oxford Univ. Press, Oxford, 2006.

[67] K. Yoshii, J. K. Anthony, and M. Katsuragawa. "The simplest route to generating a train of attosecond pulses". In: *Light: Sci. & Appl.* 2 (2013), e58.

[68] M. Katsuragawa and K. Yoshii. "Arbitrary manipulation of amplitude and phase of a set of highly discrete coherent spectra". In: *Phys. Rev. A* 95 (2017), p. 033846.

[69] T. Jannson and J. Jannson. "Temporal self-imaging effect in single-mode fibers". In: *J. Opt. Soc. Am.* 71 (1981), p. 1373.

[70] J. Azana and M. A. Muriel. "Temporal self-imaging effects: theory and application for multiplying pulse repetition rates". In: *IEEE J. on Selected Topics in Quan. Elec.* 7 (2001), pp. 728–744.

[71] J. Fatome, S. Pitois, and G. Millot. "Influence of third-order dispersion on the temporal Talbot effect". In: *Opt. Comm.* 234 (2004), pp. 29–34.

[72] D. J. Kane and R. Trebino. "Characterization of arbitrary femtosecond pulses using frequency-resolved optical gating". In: *IEEE J. Quantum Electron* 29 (1993), p. 571.

[73] M. Schultze et al. "Delay in photoemission". In: *Science* 328 (2010), pp. 1658–1662.

[74] I. A. Walmsley and V. Wong. "Characterization of the electric field of ultrashort optical pulses". In: *J. Opt. Soc. Am. B* 13 (1996), pp. 2453–2463.

[75] C. Iaconis and I. A. Walmsley. “Spectral phase interferometry for direct electric-field reconstruction of ultrashort optical pulses”. In: *Opt. Lett.* 23 (1998), pp. 792–794.

[76] T. Suzuki, N. Sawayama, and M. Katsuragawa. “Spectral phase measurements for broad Raman sidebands by using spectral interferometry”. In: *Opt. Lett.* 33 (2008), pp. 2809–2811.

Chapter 3

Experimental system

Figure 3.1 shows the main experimental system, which consists of three parts: generation of a discrete broadband spectrum, amplitude and phase manipulations, and measurement of spectral phases. The three sections below correspond to details of each part.

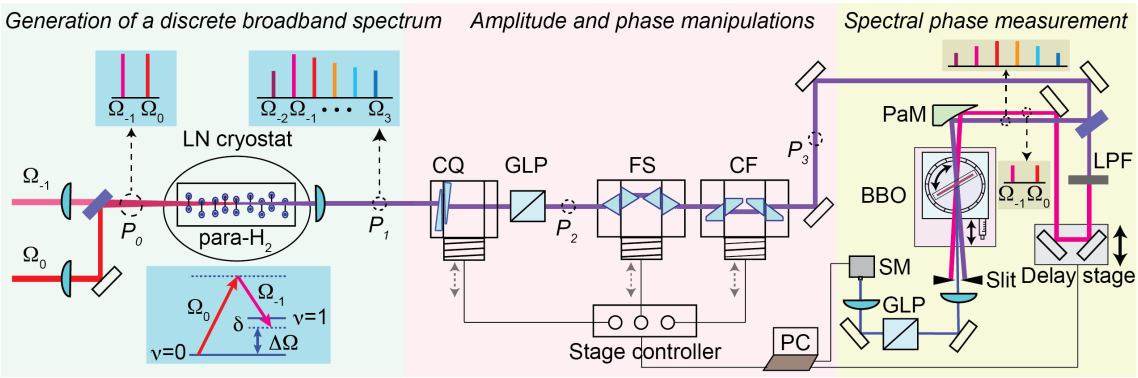

Figure 3.1: The main experimental system, consisting of three parts: generation of a discrete broadband spectrum, amplitude and phase manipulations, and measurement of spectral phases. This diagram shows a top view of the system. P_0–P_3 represent different positions on optical axis. LN, liquid nitrogen; para-H_2, para-hydrogen; CQ, crystal quartz; GLP, calcite Glan laser polarizer; FS, fused silica; CF, calcium fluoride; PaM, parabolic mirror; LPF, long-wavelength pass filter; BBO, β-barium-borate crystal (Type-1, 10 μm thick); SM, spectrometer.

3.1 Raman generation

The interaction medium – gaseous para hydrogen–is filled into an enclosed 15 cm long copper chamber, with an adiabatic temperature of 77 K, supported by a liquid nitrogen cryostat. The purity of para hydrogen is up to 99.9%.

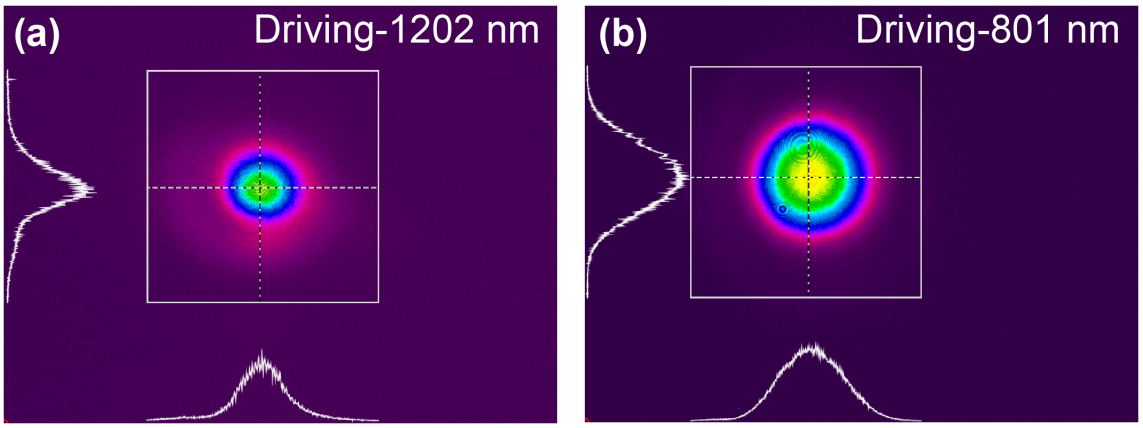

Figure 3.2: Beam profiles of two driving lasers.

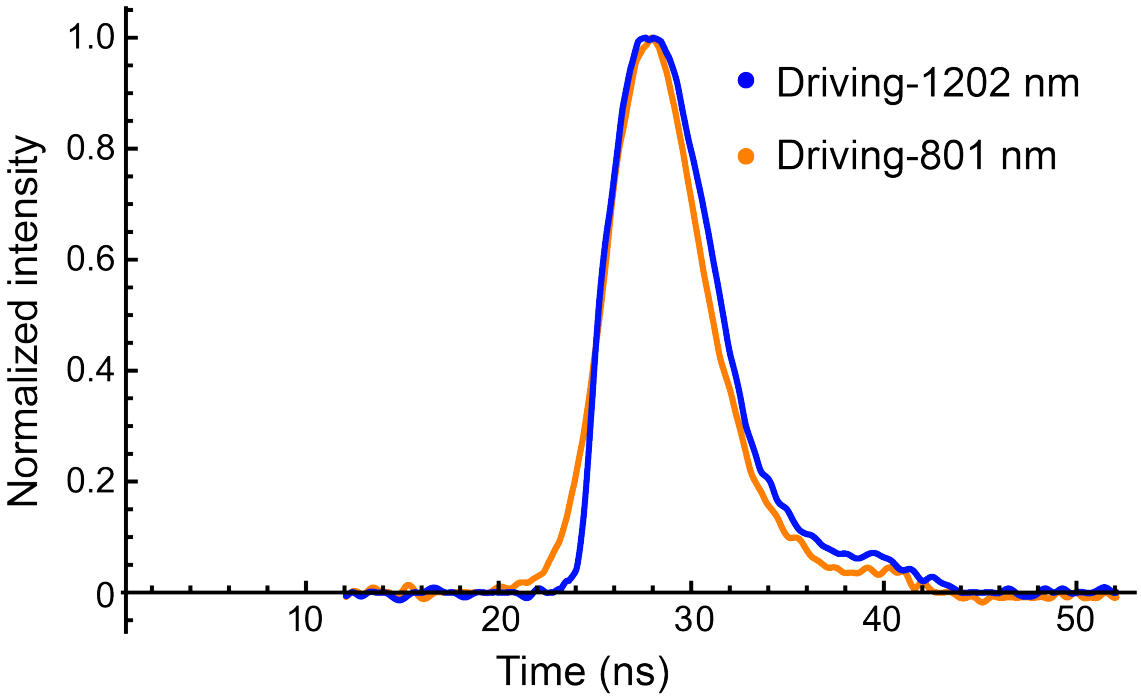

Figure 3.3: Pulse envelopes of two driving lasers. These pulse envelopes were obtained through a fast photon diode (Thorlabs DET025A), having a width of about 7 ns.

As figure 3.2 shows, two coaxial driving lasers—Ω_{-1}, 1,201.6350 nm, 6.0 mJ and Ω_0, 801.0820 nm, 6.0 mJ—have an envelope duration of about 7 ns (at full width at half maximum) and good Gaussian beam profiles. Overlapping at the chamber center of para hydrogen, the beam radii and peak intensities of Ω_{-1} and Ω_0 are 150 μm, 120 MW/cm^2 and 120 μm, 180 MW/cm^2, respectively. Two-photon detuning of vibrational Raman scattering is about δ = - 300 MHz. Refer to figure 3.3 for pulse envelopes of two driving lasers.

What to note here is that both the density of para hydrogen gas [77–79] and the lens pair of two driving lasers in front of cryostat have been carefully calibrated, for the sake of optimal Raman scattering [80]. Here, we merely use the optimal parameters: 8×10^{19} cm^{-3} for the density of para-hydrogen gas, and focal lengths of 400 mm (with respect to Ω_0) and 250 mm (with respect to Ω_{-1}) for the lens pair.

Based on the above setup, we are able to yield a series of discrete broadband

components (see the insert at position P_1), which has a constant frequency spacing of about $\Delta\Omega = \Omega_0\text{-}\Omega_{-1} = 124.75$ THz.

3.2 Manipulation devices

The middle part of figure 3.1 shows the devices of amplitude and phase manipulations. See also figure 3.4 for an enlarged view. We use a pair of wedge-shaped crystal quartz (CQ, positive uniaxial) as waveplate. The optical axis of CQ is orientated 45 degrees to the direction of linear polarization of incident laser. The transmission direction of calcite Glan laser polarizer (GLP) is set parallel to the polarization direction of incident laser. Two pairs of triangular-pole-shaped fused silica [81], and also two pairs of trapezoidal-pole-shaped calcium fluoride [82] are used for controlling phases.

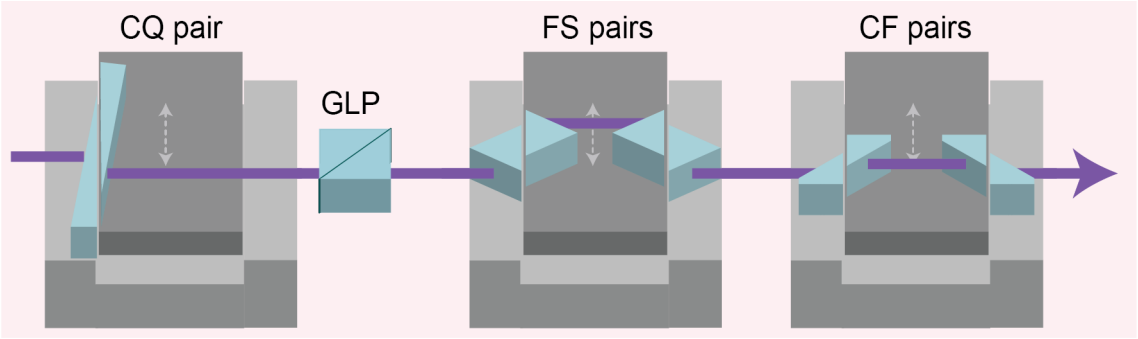

Figure 3.4: The devices of amplitude and phase manipulations. Gray dashed arrows depict translation directions of stages.

As shown in figure 3.4, all prism pairs are mounted on uniaxially movable stages (Sigma Tech FS-1020X, driven by a Sigma Tech FC-101 controller). This set of devices can translate over a range of about 20 mm, with high precision and fine resolution (about 0.1 μm), and excellent reproducibility. For convenience, the whole set of devices are controlled by LabVIEW programs. In fact, according to our analyses and experiments, the resolutions needed for precise control are about 5 μm for MA, and 1 μm for MP, respectively; and the range needed for flexible control are about 10 mm for MA, and 2 mm for MP,

respectively.

Besides, as shown in figure 3.4, all prism pairs are slightly separated by a parallel distance of 10 μm using a tungsten wire. The parallel gap is perpendicular to light propagation so that the stage can move along it to change thickness linearly.

Details of the scales of manipulation devices are shown in **Appendix A**.

Basically, we would like to perform experiments only by changing the thicknesses of waveplate and dispersive plates, hence the prisms in pairs should not shift beam path considerably after transmitting. Besides, all prisms are placed carefully to make use of their Brewster angles, through which we expect to reduce reflection loss at surfaces. Depending on spectral mode, optical path slightly shifts in parallel in some section of prism pairs, but such a shift is really a small amount and does not affect the entire propagation.

3.3 SPIDER system

The rightmost part of figure 3.1 shows SPIDER system, which is slightly modified for discrete spectra. See also figure 2.2 in chapter 2. Figure 2.2 shows a schematic diagram of SPIDER system.

Relying on frequency spacing of $\Delta\Omega$=124.75 THz, translation of the delay stage on reference arm needs to reach a resolution of about 10 nm over a range of several micrometers. The actual delay stage employed here (nPoint Inc., nPoint LC. 400) is capable of reaching a resolution of less than 1 nm over a range of more than 100 μm. Two arms of Raman components are sent through parallel paths to the parabolic mirror and con-focused onto the surface of a 10 μm thick BBO (β-barium-borate, Type-1, transmitting range of 3,500–190 nm) crystal. BBO crystal has a large nonlinear coefficient, and can be phase matched over a wide range of wavelengths. Hence it is eligible for sum frequency generation (SFG)–wavelengths from 601 to 267 nm–in our work.

The BBO crystal is mounted on to a stage with flexible adjustment, that is,

we can translate the position and twist the angle of BBO crystal for optimal phase matching.

We use a spectrometer (Ocean Optics USB 4000 or Andor SOLIS MS-257, viable wavelength range: 1,100–200 nm) to monitor intensity oscillations of SFG components (refer to figure 2.3). The translation of delay stage and the record of intensity oscillations of SFG components via spectrometer in real time are controlled by LabVIEW programs.

Nevertheless, as we expect to perform experiments to verify numerical exploration, we have to experimentally scan each point (i.e. a combination of two thicknesses) explored. This process actually yields a large quantity of raw data. Therefore, how we can translate the delay stage to scan intensity oscillations of SFG components quickly and efficiently becomes the key point whether or not this SPIDER system can be a substantial technique for retrieving phases.

Bibliography of Chapter 3

[77] J. P. Wittke and R. H. Dicke. “Redetermination of the hyperfine splitting in the ground state of atomic hydrogen”. In: *Phys. Rev.* 103 (1956), pp. 620–631.

[78] W. K. Bischel and M. J. Dyer. “Temperature dependence of the Raman linewidth and line shift for the Q(1) and Q(0) transitions in normal and para-H_2”. In: *Phys. Rev. A* 33 (1986), pp. 3113–3123.

[79] S. W. Huang, W. J. Chen, and A. H. Kung. “Vibrational molecular modulation in hydrogen”. In: *Phys. Rev. A* 74 (2006), p. 063825.

[80] K. Morimune. “Efficient generation of high-order stimulated vibrational Raman scattering”. In: *Master Thesis* (2016).

[81] I. H. Malitson. “Interspecimen comparison of the refractive index of fused silica”. In: *J. of the Opt. Soc. of Am.* 55 (1965), pp. 1205–1209.

[82] M. Daimon and A. Masumura. “High-accuracy measurements of the refractive index and its temperature coefficient of calcium fluoride in a wide wavelength range from 138 to 2326 nm”. In: *Appl. Opt.* 41 (2002), pp. 5275–5281.

Chapter 4

Results

In this chapter, I will show main experimental results, which in fact encompass three sections: results of amplitude manipulation, results of phase manipulation, and ultrafast pulses achieved. Each section consists of different number of Raman components (five, six, and seven).

Naturally, we made experiments and acquired results in sequence. That is, we started to carry out experiments from manipulating amplitudes and phases, and producing ultrashort pulses of five Raman components (spanning 2,403 to 481 nm); then did the same on six RCs (spanning 2,403 to 400 nm); and ultimately on seven RCs (covering 2,403 to 343 nm). Therefore, I will introduce the results in turn, while declaring key points and operating procedures within five RCs.

However, in fact, all the techniques of manipulation and even reconstruction of ultrafast pulses are processed in the same way for different number of Raman components. The main difference among them is that with the number of Raman components increasing, the difficulty of arbitrarily manipulating both amplitudes and phases is elevated, in terms of numerical exploring range (for MA), and experimental resolution (for MP). Detailed discussions are provided in chapter 5.

To be specific, in section 4.1, I will show the photos of Raman scattering, which is our light source to be manipulated.

In section 4.2, I will first show key points and practical procedures of manipulating amplitudes. Then I will show experimental results obtained, including actual intensity (in terms of power) and amplitude distributions achieved. As for detailed precision and error estimations, please refer to chapter 5.

In section 4.3, similarly, I will first show key points and difficulties of phase manipulation in experiment, which, comparing to MA, are more sophisticated; then list out practical procedures of MP for locking the target (i.e., near Fourier transform limited conditions); briefly show precision of phase retrieval process; and finally show the phase distribution after MP. Please also refer to chapter 5 for detailed discussions of precision in MP.

4.1 Photos of Raman components

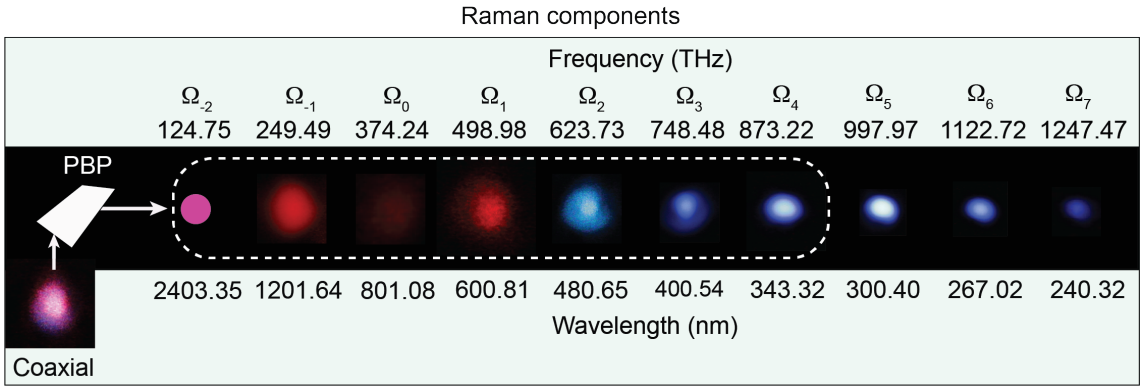

Figure 4.1: Photos of Raman components (from 1,202 to 240 nm). The red dot of 2,403 nm was not observed, and was just exhibited as a mark to represent such Raman component. PBP, pellin broca prism, which spatially separates coaxial Raman components for photo shooting; dashed line indicates the Raman components to be manipulated in experiment.

Figure 4.1 shows photos of a series of high-order Raman components [83–87], by adiabatically driven vibrational transition of para hydrogen molecules (temperature: 77 K, and density: 8×10^{19} cm^{-3}). These Raman components were generated coaxially, covering a wavelength range of 2,403 to 240 nm, i.e., Ω_{-2}

(125 THz) to Ω_7 (1250 THz), with a frequency spacing of about 125 THz. Refer to figure 4.2 for their pulse envelopes.

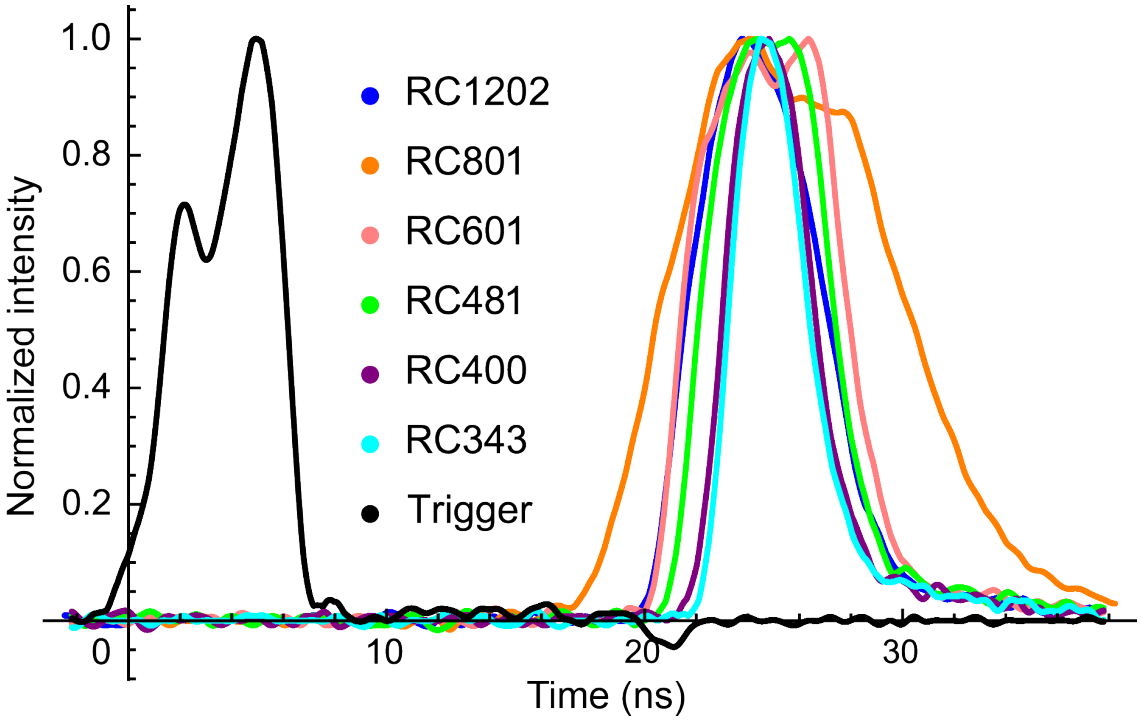

Figure 4.2: Pulse envelopes of generated Raman components. These pulse envelopes were obtained through a fast photon diode (Thorlabs DET025A). The black line shows the trigger pulse, which was scattered light of 801 nm far before para hydrogen cell

As shown in figure 4.1, the coaxial Raman components (RCs) were spatially separated by a pellin broca prism (PBP) and made incident on screens for shooting photos. All Raman components were shot one by one using a digital camera, and then trimmed by photo editor at same conditions and exhibited as in figure 4.1.

Note that in order to make beam profiles more viewable, we used different kinds of color filters when taking shots, thus recording different brightness regardless of their original intensities. We also used different kinds of screens to project each component: a normal white paper to project Raman components from 601 to 240 nm, and an infrared card to project components of 801 nm and 1,202 nm, which are in the infrared wavelength range. The component,

2,403 nm, in mid-infrared wavelength range, was not directly observed, and we simply presented it as a round spot. Because we could not capture it through proper approaches in experiment.

What is notable here is that these beams were generated efficiently and coaxially without any constraints of phase matching conditions (owing to the feature of adiabatic driving vibrational Raman coherence); had excellent Gaussian beam profiles (refer to figure 4.1); and were discrete in the frequency domain with a frequency spacing of $\Delta\Omega$ = 125 THz, which is essential and adequate for latter amplitude and phase manipulations.

Given the above brilliant light source–a highly discrete broadband spectrum with good Gaussian beam profiles, we could move on to manipulating its amplitudes and phases.

4.2 Results of amplitude manipulation

This section shows results of amplitude manipulation on five, six, and seven Raman components, respectively. I will begin with five RCs. Meanwhile, I will show key points of implementing experiments, concrete procedures of manipulating amplitudes, and finally exhibit achieved amplitudes. Afterwards, I will show similar results of six and seven Raman components.

4.2.1 Results of amplitude manipulation of five Raman components

Using the device of amplitude manipulation shown in figure 3.4, we carried out experiments to tailor all intensities (in terms of power).

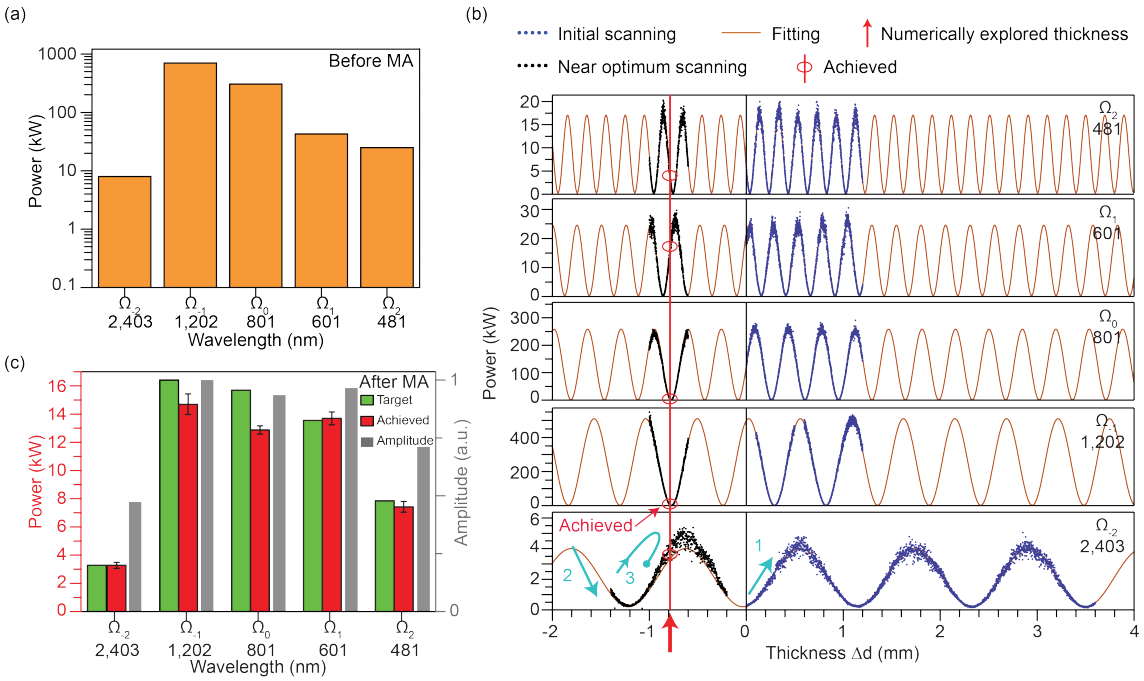

Figure 4.3: Results of amplitude manipulation of five Raman components. (a), Original powers of five Raman components. Ω_{-2}, 8.0; Ω_{-1}, 704.3; Ω_0, 305.7; Ω_1, 42.9; Ω_2, 25.0 (kW), respectively. (b), MA process. Cyan numbers with arrows in Ω_{-2} indicate manipulating process: 1, initial scanning for determining basic parameters of power oscillations; 2, fitting with sinusoidal functions according to initial scanning; 3, experimental exploration of the optimum around the numerically expected optimal thickness. (c), Target (green) and achieved (red) power distributions. (Raman component: target (kW), achieved (kW)): (Ω_{-2}: 3.3, 3.3), (Ω_{-1}: 16.4, 14.7), (Ω_0: 15.7, 12.9), (Ω_1: 13.6, 13.7), (Ω_2: 7.9, 7.4), respectively; gray columns indicate achieved amplitude distribution normalized by the maximal intensity of Ω_{-1}. Typical power fluctuations are in a range of about $\pm 3\%$– $\pm$ 7%, marked as error bars (standard deviations) above the red columns.

As shown in $\log_{10}$-scale in figure 4.3(a), the original powers of five Raman components before manipulating were Ω_{-2}, 8.0; Ω_{-1}, 704.3; Ω_0, 305.7; Ω_1, 42.9; Ω_2, 25.0 (kW), respectively. These powers were measured directly by an energy meter (Ophir NOVA 2), with an envelope duration of about 7 ns. Also refer to figure 4.1. The powers before MA are vastly different from each other, even

with different levels–from the lowest 8 kW to the highest 704 kW. Given such preconditions, through MA process, we expect to achieve near flat intensities and thus near flat amplitudes, which contribute to reconstructing ultrafast pulses. As a result, we set near flat distribution of intensity (or amplitude) as our target.

To realize our target, basically, the adjustment would be the direction of decreasing powers, namely, maintaining the powers of Ω_{-2} and Ω_2–which were very low–to their maximal values, and meanwhile suppressing powers of the rest components.

What is worth noting is that although here we set near flat distribution of powers for producing ultrafast pulses, we are actually able to arbitrarily manipulate these intensities, i.e., to produce some complex distributions. Nevertheless, when the complexity of target distribution increases, we have to extend the range of numerical exploration to approach such target. That is, the difficulty of MA escalates following the complexity of target distribution.

As an optical technology in practical use, the difficult point is that we can not directly and analytically calculate intensity oscillations and further predict where to find the exact solution. Instead, we numerically explore an approximate solution that approaches the target well with high precision. Below shows how we were able to realize such idea.

To numerically explore optimal solution for the intensity distribution of target, we have to grasp concrete behaviors of power oscillations of all five (later six and seven) Raman components over a wide range. As discussed in chapter 2, the power of each Raman component oscillates periodically with respect to the thickness of waveplate (i.e., CQ pair).

In general, first we can sweep through a range of a few millimeters of waveplate thickness (initial scanning). Next we can fit initial scanning with sinusoidal functions, and obtain basic parameters of each oscillation–period and initial intensity. Then we can predict intensity oscillations of all RCs over a fairly wide range (far beyond the range of initial scanning). That is to say, we can numerically explore an optimal thickness to approach the target over a

very wide range. At the determined optimal thickness, the power distribution is supposed to approach the target very well. Normally, the range of numerical exploration extends very far; however, by chance it can happen to be found nearby the starting position.

Besides, to verify accuracy of the fit and explored optimal thickness, we should particularly sweep a mini range incorporating the explored optimal thickness. If the mini range of scanning does not match the former fit, we have to abandon such optimal thickness. Because it may out-range the limit of manipulating (within about $\pm$10 mm) and gives rise to incorrectness at such position. We have to repeat the process of numerical exploration again and determine a new optimal thickness.

Hereby, we take the case of manipulating amplitudes of five Raman components as a typical example, and list comprehensive procedures of operation.

Before manipulating, we set powers of the target as: Ω_{-2}, 3.3; Ω_{-1}, 16.4; Ω_0, 15.7; Ω_1, 13.6; and Ω_2, 7.9 (kW), respectively. See green columns in figure 4.3(c).

To achieve the above target, first, we swept a range of CQ thickness (3.6 mm with a moving speed of 12 μm/s for Ω_{-2}, and 1.2 mm with a moving speed of 4 μm/s for the rest Raman components) to obtain power oscillations. These oscillations are shown as blue dots in figure 4.3(b). We controlled translation of the stage of CQ via LabVIEW programs, and monitored intensity oscillations of different Raman components one by one via energy meter (Ophir NOVA 2), which was also connected to a PC and operated by LabVIEW programs. The LabVIEW programs were designed delicately to control speed and range of translation, and record intensities in real time.

Second, we fit above scanning with sinusoidal functions (fitting standard errors $<$1%), which are shown as brown lines. Periods of the fit are (Ω_{-2}–Ω_2) 1.178, 0.532, 0.345, 0.253, and 0.198 (mm), which differed $<$3% from theoretical results. Theoretical periods regarding crystal quartz are (Ω_{-2}–Ω_2) 1.277, 0.549, 0.354, 0.260, and 0.202 (mm), respectively. The deviation of 2,403 nm (Ω_{-2}) is larger, due to wavelength limit of Sellmeier equation. Refer to chapter

5 for precision discussions.

Third, based on fitting functions, we explored an optimal thickness to approach the target. We found that at thickness of -0.7996 mm (comparing to the thickness of origin, 0 mm), the power distribution (red thick line in figure 4.3(b) approaches the target the best. The differences from the exploration to the target are in a range of 1% to 4%. Obviously, these explored powers are very close to the target.

Fourth, we swept a mini range of $\pm$0.2 mm (with a moving speed of 4 μm/s), centering at the explored optimal thickness, to validate the fit. The mini range of scanning is shown as black dots in figure 4.3(b). Apparently, the black dots agree well with fitting lines (brown), which means that it is secure to lock such position as the optimum.

Finally, we translated crystal quartz to the optimal thickness (-0.7996 mm), and measured practical powers. As shown in figure 4.3(c), red columns indicate actually achieved powers: Ω_{-2}, 3.3; Ω_{-1}, 14.7; Ω_0, 12.9; Ω_1, 13.7; and Ω_2, 7.4 (kW), respectively. Error bars above red columns are due to intensity fluctuations of Raman generation, which are estimated in a range of $\pm$3%–$\pm$7%. Deviations from achieved results to the target are Ω_{-2}, 0; Ω_{-1}, 6%; Ω_0, 19%; Ω_1, 0; and Ω_2, 13%, respectively. Also refer to chapter 5 for discussions of precision.

The amplitude distribution of five Raman components based on achieved intensities is shown as grey columns in figure 4.3(c). Such amplitude distribution is normalized with respect to the strongest component Ω_{-1}. It is a near flat amplitude distribution.

The evaluations of results of MA on five Raman components are detailed in chapter 5, mainly through precision estimating of fitting lines; precision of achieved powers; and the influence of MA to generating ultrafast pulses.

4.2.2 Results of amplitude manipulation of six Raman components

With one more component, 400 nm (Ω_3) added to the above Raman components, we used the same device to manipulate amplitudes of six RCs. Below shows detailed results.

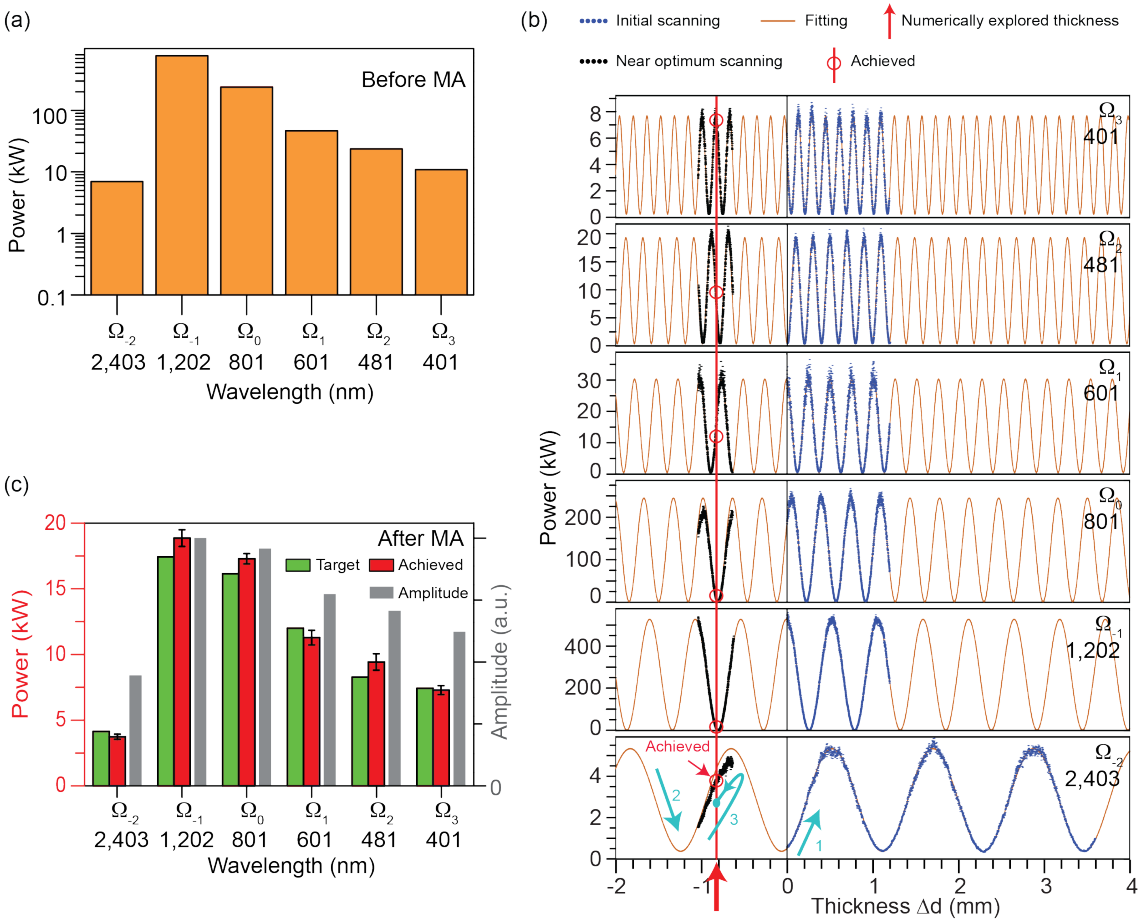

Figure 4.4: Results of amplitude manipulation of six Raman components. (a), Original powers of six Raman components before MA. Ω_{-2}, 7.1; Ω_{-1}, 775.7; Ω_0, 240.9; Ω_1, 45.9; Ω_2, 24.3; Ω_3, 10.9 (kW), respectively. (b), Exploration of the optimal thickness of CQ. Cyan numbers with arrows in Ω_{-2}: 1, initial scanning for determining basic parameters of power oscillations of six RCs; 2, fitting according to initial scanning; 3, route of locking the optimal thickness. (c), Target (green) and achieved (red) power distribution. (Raman component: target (kW), achieved (kW)): (Ω_{-2}: 4.1, 3.7), (Ω_{-1}: 17.4, 18.9), (Ω_0: 16.1, 17.3), (Ω_1: 12.0, 11.3), (Ω_2: 8.3, 9.4), (Ω_3: 7.4, 7.3), respectively; gray columns indicate amplitude distribution according to achieved power distribution, which is normalized based on Raman component, Ω_{-1}. Typical power fluctuations are in a range of about $\pm 3\%$– $\pm\ 7\%$, marked as error bars (standard deviations) above red columns.

Figure 4.4(a) shows original power distribution of six high-order Raman

components in $\log_{10}$-scale. From Ω_{-2} to Ω_3, the powers are 7.1, 775.7, 240.9, 45.9, 24.3, and 10.9 (kW), respectively. As discussed before, we expected to 'flatten' power distribution to some extent for generating ultrafast pulses. Therefore, we would like to mainly suppress high powers of RCs, Ω_{-1} to Ω_0, and retain low powers of Ω_{-2} and Ω_3.

We set power distribution of the target to Ω_{-2}, 4.1; Ω_{-1}, 17.4; Ω_0, 16.1; Ω_1, 12.0; Ω_2, 8.3; and Ω_3, 7.4 (kW), shown as green columns in figure 4.4(c).

Refer to figure 4.4(b). Following the same procedures of MA as in the case of five Raman components, we found that at the thickness of -0.8256 mm, the power distribution approached the target the most. The differences from the explored to the target are about 1% and considered negligible.

Next, we swept a mini range of $\pm$0.2 mm (with a moving speed of 4 μm/s), centered at the explored thickness, to validate the fitting lines. See black dots in figure 4.4(b). These black dots are consistent with fitting lines (brown), which means that it is permissible to lock such position as the optimum.

Finally, we moved the thickness of CQ pair to - 0.8256 mm and measured actual powers (red columns in figure 4.4(c)), which are very close to the target. The powers measured at the optimal thickness are Ω_{-2}, 3.7; Ω_{-1}, 18.9; Ω_0, 17.3; Ω_1, 11.3; Ω_2, 9.4; and Ω_3, 7.3 (kW), respectively.

Deviations of powers from the "achieved" to the "target" are Ω_{-2}, 10%; Ω_{-1}, 8%; Ω_0, 7%; Ω_1, 6%; Ω_2, 14%; and Ω_3, 2%, respectively. Refer to chapter 5 for discussions of precision.

Error bars are also shown above the achieved powers (red columns), which indicate intensity fluctuations of generated high-order Raman series in a range of about $\pm$3%–$\pm$7%.

Based on achieved power distribution, we were able to calculate amplitude distribution normalized by the maximal intensity of Ω_{-1}. Gray columns in figure 4.4(c) show the normalized amplitude distribution, which is nearly 'flat'.

4.2.3 Results of amplitude manipulation of seven Raman components

Comparing to six Raman components, which span 2,403 nm over to 400 nm, we increased one more component, 343 nm (Ω_4) to the broadband spectrum and improved the level of amplitude manipulation.

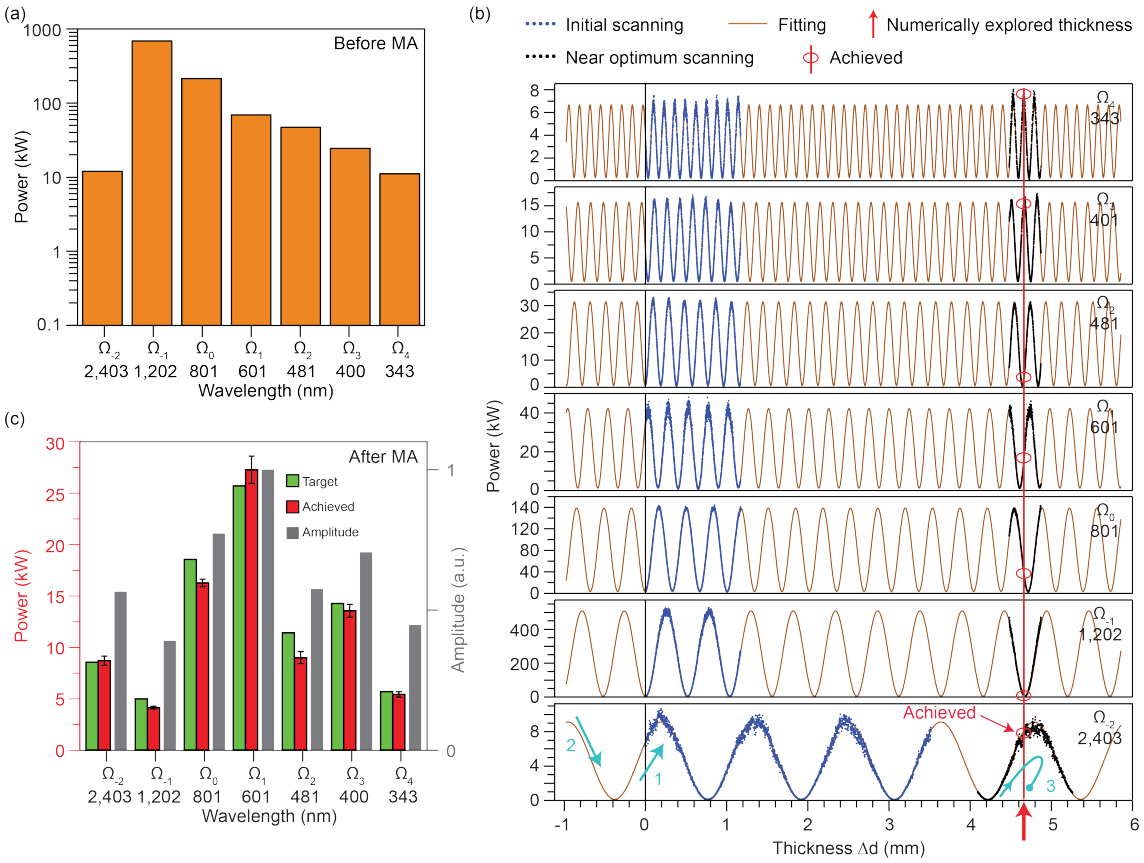

Figure 4.5: Results of amplitude manipulation of seven Raman components. (a), Original powers of seven Raman components before MA: Ω_{-2}, 12.0; Ω_{-1}, 692.9; Ω_0, 215.0; Ω_1, 69.6; Ω_2, 47.1; Ω_3, 24.6; Ω_4, 11.1 (kW), respectively. (b), Exploration of the optimal thickness of CQ. Cyan numbers with arrows in Ω_{-2}: 1, initial scanning for determining basic parameters of power oscillations; 2, fitting lines according to initial scanning; 3, route of locking the optimal condition. (c), Target (green columns) and achieved (red columns) power distribution. (Raman component: target (kW), achieved (kW)): (Ω_{-2}: 8.6, 8.7), (Ω_{-1}: 5.0, 4.1), (Ω_0: 18.6, 16.3), (Ω_1: 25.7, 27.3), (Ω_2: 11.4, 9.0), (Ω_3: 14.3, 13.6), (Ω_4: 5.7, 5.4), respectively; gray columns indicate achieved amplitude distribution normalized by the maximal intensity of Ω_1. Typical power fluctuations are in a range of about $\pm 3\%$–$\pm 7\%$, marked as error bars (standard deviations) above red columns.

As shown in figure 4.5(a), original powers of seven Raman components are Ω_{-2}, 12.0; Ω_{-1}, 692.9; Ω_0, 215.0; Ω_1, 69.6; Ω_2, 47.1; Ω_3, 24.6; and Ω_4, 11.1 (kW),

respectively. Similar to the case of five and six Raman components, this power distribution before manipulation of amplitudes also covers a wide scope, with different levels of powers involved.

For manipulating amplitudes of seven Raman components, we set powers of the target as Ω_{-2}, 8.6; Ω_{-1}, 5.0; Ω_0, 18.6; Ω_1, 25.7; Ω_2, 11.4; Ω_3, 14.3; and Ω_4, 5.7 (kW), respectively. See green columns in figure 4.5(c).

Following the same procedures of manipulating amplitudes as in former subsections, we explored and locked the optimal thickness of CQ pair at 4.7947 mm. The differences of powers from the explored to the target are in a range of only 1% to 5%.

We also swept a mini range of $\pm$0.2 mm (with a moving speed of 4 μm/s), centering at the explored thickness, to validate fittings. See black dots in figure 4.5(b). These black dots are consistent with the fitting lines (brown), therefore, it was eligible to lock such position as the optimum.

Adjusting the thickness of CQ pair to the explored optimal value, we measured the actual powers: Ω_{-2}, 8.7; Ω_{-1}, 4.1; Ω_0, 16.3; Ω_1, 27.3; Ω_2, 9.0; Ω_3, 13.6; and Ω_4, 5.4 (kW), respectively. See red columns in figure 4.5(c).

Deviations of powers from the "achieved" to the "target" are Ω_{-2}, 2%; Ω_{-1}, 17%; Ω_0, 12%; Ω_1, 6%; Ω_2, 21%; Ω_3, 5%; and Ω_4, 5%, respectively.

Error bars are also shown above achieved power distribution in figure 4.5(c), which were due to intensity fluctuations of generated high-order Raman components.

Normalized amplitude distribution based on achieved powers is shown as grey columns in figure 4.5(c).

Refer to chapter 5 for detailed discussions on precision, and detailed comparison of amplitude manipulation on five, six, and seven Raman components.

4.3 Results of phase manipulation

After manipulating amplitudes to a nearly 'flat' distribution, we could move on to manipulating phases.

What is noteworthy here is that the experiments of MA and MP were somehow independent, thus allowing us to conduct experiments of MA and MP on different days. Generally, when manipulating phases, the normalized amplitudes of Raman components were in accordance with the results of MA, in spite of different days with slightly different conditions of Raman generation. In other words, for the same number of Raman components, the exact powers of them might be slightly different from the day of MA to the day of MP, while the normalized amplitudes for both MA and MP remained almost the same. Refer to chapter 5 for detailed discussions. This principle is critical, because the ideas of MA and MP need to be combined to construct ultrafast pulses near Fourier transform limited condition, and we cannot single out either MA or MP for that purpose.

Through manipulating spectral phases, we expected to achieve a distribution of phases close to zero radians for different number of Raman components. Resembling the case of amplitude manipulation, I will show results of phase manipulation on different number of Raman components, from five to six, and eventually to seven. Key points and specific procedures of MP will be recounted in the case of five Raman components.

4.3.1 Results of phase manipulation of five Raman components

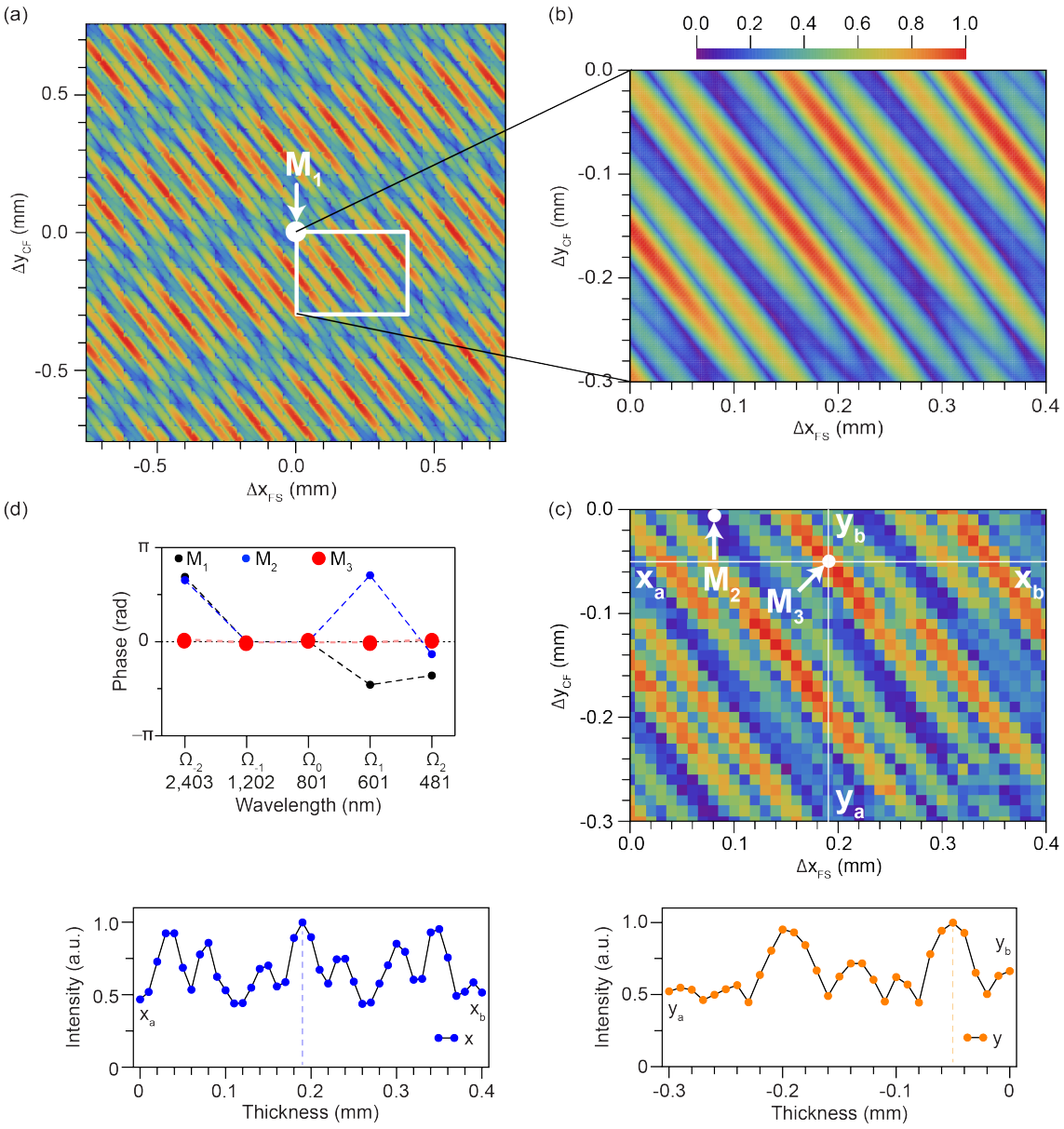

Figure 4.6: Results of phase manipulation of five Raman components. (a), Calculated 2D plot of peak values of electric field intensity waveforms as functions of thicknesses of fused silica (Δx_{FS}) and calcium fluoride (Δy_{CF}) within a range of 1×1 mm^2. White rectangle indicates the maximal range to be verified in experiment. Point M_1 indicates initial condition determined experimentally.

Figure 4.6: (Previous page.) (b), Enlarged 2D plot of the range (0.4×0.3 mm^2) indicated by the white rectangle in (a). (c), 2D plot of observed peak values of electric field intensity waveforms, in which we explored the range corresponding to that in (b) with a resolution of 0.01 mm and 41×31 points. Point M_2 indicates a reference point which has a low peak intensity and is far from the optimum. Point M_3 indicates optimal point determined experimentally. (d), Spectral phases observed at positions M_1 (initial position, black), M_2 (weak position, blue), and M_3 (optimal position, red), respectively. Pink line (least square fit) shows linear fitting of the spectral phases at M_3. (e), Plot of peak intensities along x_a–x_b (blue dots) axis including point M_3. (f), Plot of peak intensities along y_a–y_b (orange dots) including point M_3.

Figure 4.6 shows main results of phase manipulation on five Raman components.

As introduced in equation 2.26 in chapter 3, by moving delay stage on the arm of reference in the SPIDER setup to sweep delay time τ, we acquired the first raw data of intensity oscillations of interfered SFG components. Figure 2.3(b) shows typical examples of raw data of intensity oscillations of interfered SFG components. In experiment, during every sweep where we observed intensity oscillations of SFG components, we moved delay stage in 100 steps—each step with 36 nm—to accumulate a delay distance of 7.2 μm (doubled moving distance because of round trip). Taking into account frequency spacing of $\Delta\Omega$=125 THz, in this 'travel', we actually obtained three periods (τ=24.06 fs) of sinusoidal intensity oscillations of interfered SFG components. In this process, we also designed LabVIEW programs to control translation of delay stage, stages of FS and CF, in terms of speed (i.e., resolution) and range. In the mean time, the spectrometer (Ocean Optics USB 4000 or Andor SOLIS MS-257) was also connected to PC and used to monitor intensity oscillations of interfered SFG components via LabVIEW programs. Refer to figure 4.7 for the raw data.

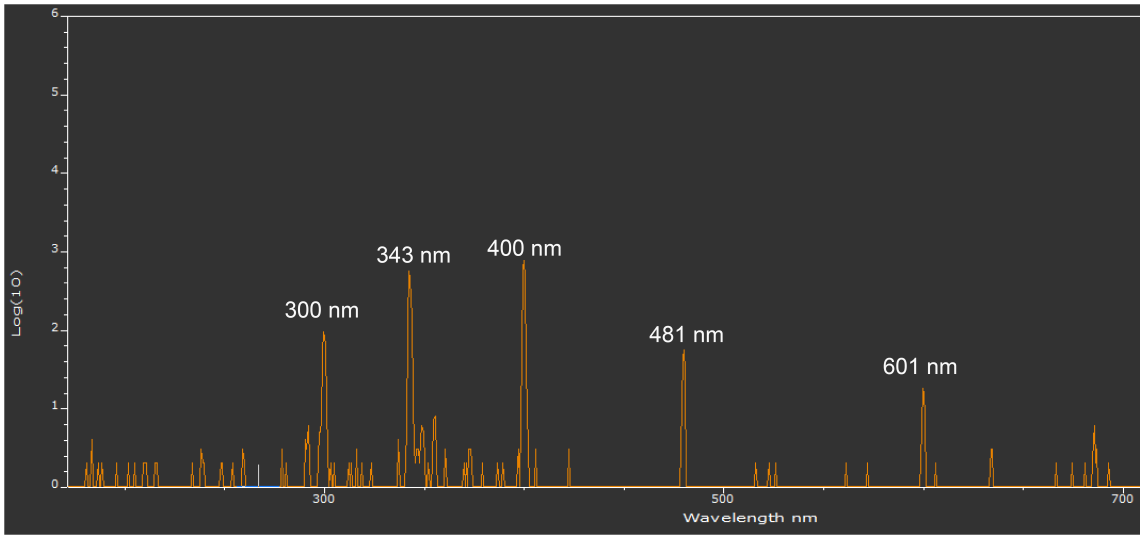

Figure 4.7: Intensities of interfered SFG components obtained from spectrometer.

Then we fit the first raw data (initial point, M_1) with sinusoidal functions for all four interfered SFG components. In this process, we were able to extract spectral phases of these SFG components, which are (confined within -π–+π) Ω_1, -1.663; Ω_2, 2.457; Ω_3, -2.389; and Ω_4, 2.149 (rad), respectively.

Precision of the fitting is very crucial, because the foundation of entire SPIDER system relies on phase retrieval of interfered SFG components. Thus here we have to evaluate precision of the fitting lines (See chapter 5 for detailed discussions). Standard errors of the fitting lines are in a range of about 3%–13%, due to intensity fluctuations of Raman generation. Basically, nonlinear processes, such as sum frequency generation, are sensitively affected by fundamental intensity fluctuations. Especially, the two SFG components on the edge, which were generated from too low or too high-order Raman modes, had larger fluctuations compared to the rest modes. However, as experimentally proved, such degree of intensity fluctuations, fortunately, was allowable for phase retrieval and thus MP.

Next, according to the interfering process in equation 2.26, we were able to retrieve initial phases of fundamental Raman components. Comparing against interfered “SFG components”, here we used the term “fundamental” for the

spectrum before sum frequency generation. Note that we used a trick to revert phases of fundamental Raman components by defaulting two of them as zero rad. This trick made sense because when it relates to high-order dispersions of a spectrum in a dispersive material, we can ignore the zeroth and first orders of dispersions while keeping the pulse shape unaltered. Hence, we were able to make any two fundamental phases as zero rad. We here chose the phases of Ω_{-1} and Ω_0) to be zero rad. In this sense, the five fundamental phases retrieved (confined to -π–+π) were Ω_{-2}, 2.163; Ω_{-1}, 0; Ω_0, 0; Ω_1, -1.436; and Ω_2, -1.128 (rad), where both thicknesses (of FS and CF) originated from 0 mm. Apparently, the distribution of initial fundamental phases was far from the line of zero rad. Therefore, we expected to 'flatten' them to zero rad through the process of phase manipulation.

With retrieved fundamental phases of the initial point, according to equation 2.25, we were able to alter these phases by adjusting thicknesses of FS and CF. In other words, through shifting two thicknesses, we could calculate how phases change at the output of MP device, and thus expect to find an optimal combination of thicknesses where all fundamental phases approach zero rad.

However, here we have to clarify the difficulties of manipulating phases, which are somehow similar to those of manipulating amplitudes. Although it is clear that approximate solutions to the target appear with a certain frequency (due to cycle of 2π of phase), it is difficult to analytically predict where the optimal solution actually appears. Mimicking the case of MA, first and foremost, we have to numerically explore approximate solutions over a wide range with high precision. Then through experimental scanning, we should verify the accuracy of numerical exploration. Finally we can lock the optimal position close to the target in experimental scanning. This is the basic approach of phase manipulation.

In the meantime, it is natural to plot all fundamental phases during the process of phase retrieving. However, that will be a vast amount of work and not easy to exhibit. Instead, according to Fourier transformation, the peak values of electric field intensity waveforms—configured by spectral phases and known electric-field amplitudes—can be plotted as functions of thicknesses of fused silica and calcium fluoride for convenience. Therefore, the target of

achieving 'flat' distribution of phases is substituted by determining a point, at which the peak value of electric field intensity waveforms is the maximal, close to unity when normalized as in equation 2.27.

Besides, during experiment of acquiring peak intensities, we have to scan each point to obtain intensity oscillations of interfered SFG components. This is technically a very high hurdle, in terms of precision of exploring and time consumption. For the same area of peak intensities (refer to4.6(a)), the finer the resolution is when adjusting two thicknesses, the more precisely we can approach the target; however, the more time it will consume to complete such scanning in experiment. For instance, in a range of 0.2×0.2 mm^2, the time it takes to scan with a resolution of 0.001 mm is one hundred times than that with a resolution of 0.01 mm, and just the latter case takes around two hours for completing the scanning. Therefore, we have to choose a suitable resolution according to the range of scanning.

So far, the key point of implementing phase manipulation turns to numerically determining a range with appropriate size and scanning it in experiment with suitable resolution. Through this process, we expected to experimentally determine an optimal point with the maximal peak intensity.

According to the first raw data and retrieved fundamental phases, we calculated the normalized peak intensity of the starting point, 0.748 (See point M_1 in figure 4.6(a)). As described earlier, we swept thicknesses of FS and CF to calculate and predict how the intensities would change over a rather wide range. Figure 4.6(a) shows a wide area numerically explored, which is 1×1 mm^2.

As shown in figure 4.6(a), quasi-periodical behavior of peak intensities of fundamental components as functions of thicknesses of FS and CF was confirmed. Note that the intensities calculated in this 'map' were not exactly periodical but very complex to be somehow quasi-periodical, which certified the fact that we could not analytically settle the optimal position. Moreover, this map was too large to be scanned in experiment with a suitable resolution. We had to focus on a smaller size within this map and experimentally scan it with a proper resolution.

The white frame in figure 4.6(a) indicates a reduced size of distribution of peak intensities as functions of thicknesses of FS and CF that we chose to verify in experiment. Although the choice of determining an area to scan in experiment could be slightly different, at least if we searched the whole area in the white frame, we could expect that an approximate solution to the target (i.e., peak intensity close to unity) would appear at a point inside the white frame.

Figure 4.6(b) is an enlarged view of the white frame in figure 4.6(a), which is 0.4×0.3 mm^2, much smaller than the size of figure 4.6(a). Figure 4.6(b) was recalculated with an increased resolution. In this map of peak intensities, we can see a few red and narrow "stripes", among which we aimed to find approximate solutions.

Referring to the map of peak intensities predicted in figure 4.6(b), we conducted experiment to confirm its accuracy: the peak values of electric field intensity waveforms were picked up and then plotted as functions of thicknesses of FS and CF in figure 4.6(c). We scanned the map of peak intensities in figure 4.6(c) with a resolution of 0.01 mm, including 41×31 points.

Comparing figure 4.6(c) with 4.6(b), we could actually confirm that the behaviors of observed peak intensities as functions of thicknesses of FS and CF were in good agreement with numerical calculation. This implies feasibility of our method of phase manipulation: first, numerically exploring; second, experimentally confirming; third, locking an approximate solution based on experimental results.

According to the results obtained in figure 4.6(c), we determined the optimal combination of two thicknesses at point M_3, with a resolution of 0.01 mm. The peak intensity at M_3 (0.998) approached the target the most. Certainly, as assumed before, the optimal position, M_3 was located inside one of the red and narrow stripes.

We could roughly ascertain our hypothesis that the peak intensity at point M_3 is the maximum by plotting peak intensities along two axes including point M_3. Figure 4.6(e) and 4.6(f) show distributions of peak intensities along x_a–x_b

(blue dots) and y_a–y_b (orange dots) axes at M_3, respectively. Apparently, the highest peak intensity alongside either axis of M_3 emerged at the intersection, M_3.

Figure 4.6(d) shows phase distributions at three representative positions. M_1 (black) was the initial point before the process of MP, where we started numerical exploration. M_2 (blue) was a point with low peak intensity and far from the optimum, which we regarded as a reference. And M_3 (red) was the optimal point we determined experimentally. By contrast, the phases at both M_1 and M_2 distributed messily and were far away from zero rad; while the phases at M_3 was the closest to zero rad of the three points. Pink line is a linear fitting of spectral phases at M_3. In fact, at the optimal point, M_3, near linear phase distribution (close to zero rad) was achieved, which prompted to reconstruct ultrafast pulses near Fourier transform limited condition. Spectral phases after subtracting linear relation at point M_3 were: Ω_{-2}, 0.034; Ω_{-1}, - 0.050; Ω_0, 0.029; Ω_1, - 0.045; Ω_2, 0.032 (rad).

Till now, for phase manipulation, through numerically exploring and experimentally verifying distribution of peak intensities as functions of thicknesses of FS and CF only once, we were able to lock the optimal point, M_3, which approached the target the best in the achieved intensity 'map'.

Refer to chapter 5 for discussions of precision during the process of MP.

4.3.2 Results of phase manipulation of six Raman components

This subsection shows the results of phase manipulation of six Raman components (2,403–400 nm).

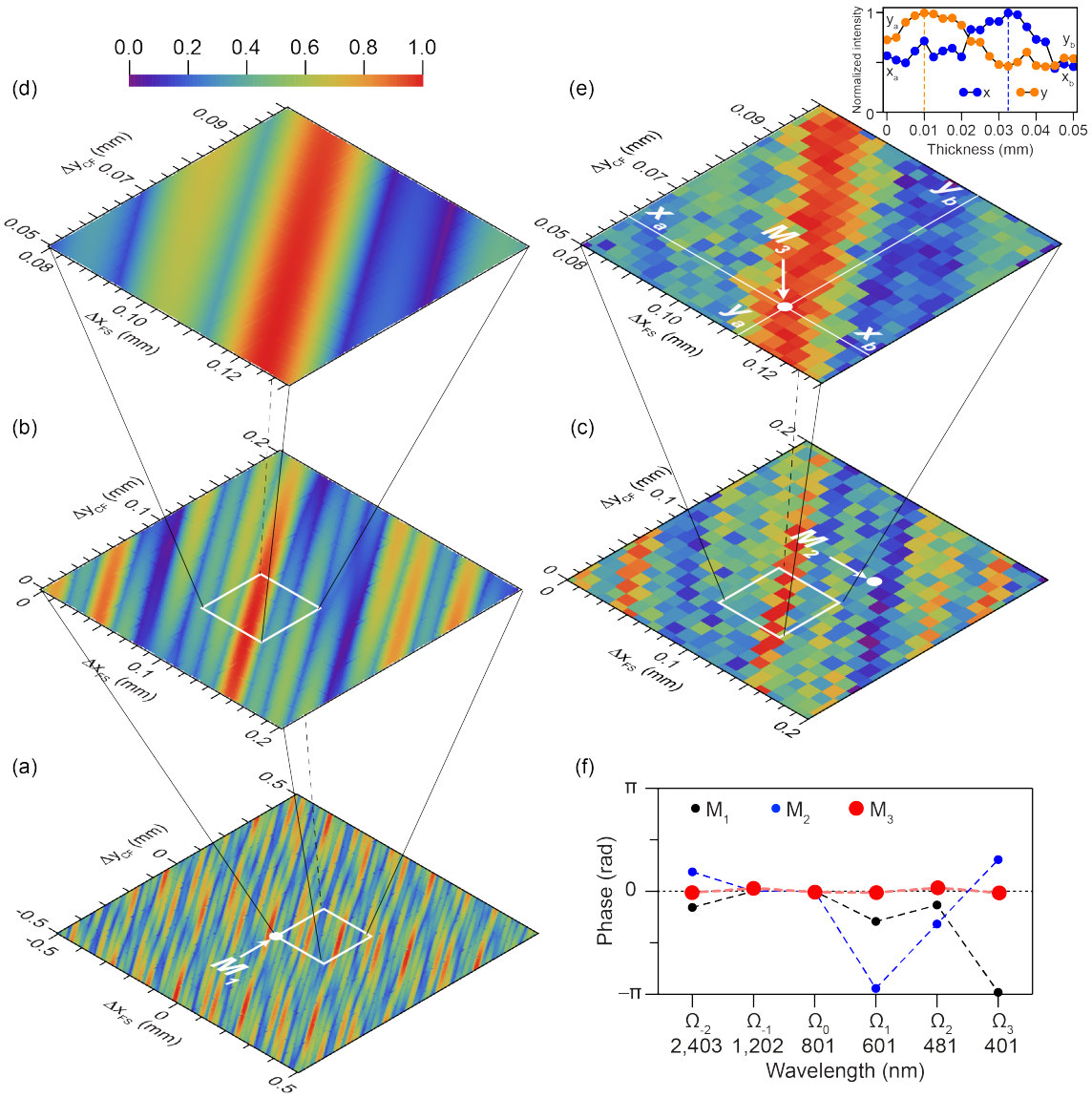

Figure 4.8: Results of phase manipulation of six Raman components. (a), Calculated 2D plot of peak values of electric field intensity waveforms as functions of fused silica (Δx_{FS}) and calcium fluoride (Δy_{CF}) thicknesses within a large range of 1×1 mm^2. The white rectangle indicates the maximal range to be verified in experiment. Point M_1 indicates the initial condition determined experimentally. (b), Enlarged 2D plot of the area (0.2×0.2 mm^2) indicated by the white rectangle in (a). The white rectangle indicates the focused area again to be verified in experiment. (c), 2D plot of observed peak values of electric field intensity waveforms, in which we explored the area corresponding to that in (b) with a resolution of 0.01 mm and 21×21 points.

Figure 4.8: (Previous page.) Point M_2 indicates a reference point which has a very low peak intensity and is far from the optimum. (d), Enlarged contour plot of the area (0.05×0.05 mm^2) indicated by the white rectangle in (b). (e), Contour plot of the observed peak values of electric field intensity waveforms, in which we explored the area corresponding to that in (d) with a resolution of 0.0025 mm and 21×21 points. Point M_3 indicates the optimal point determined experimentally. The plot next to (e) indicates distributions of peak intensities alongside two axes of point M_3: x_a–x_b (blue dots) and y_a–y_b (orange dots), respectively. (f), Spectral phases observed at positions M_1 (initial position, black), M_2 (weak position, blue), and M_3 (optimal position, red), respectively. Pink line (least square fit) shows linear fitting of the spectral phases at M_3.

With six Raman components, by moving delay stage on the arm of reference to sweep delay time, τ, we acquired the first raw data of intensity oscillations of five interfered SFG components. In this scanning, we moved delay stage in 100 steps, with each step moving 0.036 μm to obtain three periods of sinusoidal oscillations for all interfered SFG components.

Then we fit the first raw data with sinusoidal functions for all five SFG components. In this process, we extracted SFG phases of the first raw data, which are (confined within -π–+π) Ω_1, 2.383; Ω_2, 2.877; Ω_3, -2.485; Ω_4, 2.377; and Ω_5, -0.741 (rad), respectively. Fitting standard errors of the raw data, which were due to intensity fluctuations of Raman generation, are the same as the case of five Raman components.

Then we retrieved the phases of six fundamental RCs according to equation 2.26 (confined to -π–+π): Ω_{-2}, -0.494; Ω_{-1}, 0; Ω_0, 0; Ω_1, -0.921; Ω_2, -0.421; and Ω_3, -3.086 (rad), respectively.

With these retrieved phases of fundamental RCs, we calculated the normalized intensity of such initial point, which is 0.634 (shown as M_1 in figure 4.8(a)). As described earlier, we adjusted thicknesses of FS and CF to calculate and predict how the intensities would change over a rather wide area–1×1 mm^2 in figure 4.8(a). White frame in figure 4.8(a) indicates a reduced size of distribution of peak intensities that we determined to verify in experiment.

Figure 4.8(b) is an enlarged view of the white frame portion in figure 4.8(a), which is 0.2×0.2 mm^2, only 1/25 of the size of figure 4.8(a). In this 'map', we could see a red and narrow 'stripe', inside which we expected to find an approximate solution to the target.

Following the 'map' of peak intensities predicted in figure 4.8(b), we conducted experiment to confirm its accuracy. The peak values of electric field intensity waveforms were picked up and plotted as functions of thicknesses of FS and CF, shown as figure 4.8(c). The resolution chosen for adjusting two thicknesses was 0.01 mm, making 21×21 points in figure 4.8(c). As expected, figure 4.8(c) and 4.8(b) were in good agreement, which certified correctness of numerical exploration with six Raman components.

However, the resolution in the area of figure 4.8(c) was not adequate enough for obtaining an approximate solution. We had to narrow down the area of searching (white frame in figure 4.8(b)) again, and correspondingly improve the resolution of adjustment of two thicknesses for finding an approximate solution. The maximal peak intensity in figure 4.8(b) is 0.968.

Figure 4.8(d) (0.05×0.05 mm^2) shows an enlarged view of the white frame in figure 4.8(b). The former was only 1/16 the size of the latter. By far, we refined the area of exploring twice and made it 1/400 the size of initial map (figure 4.8(a)). In figure 4.8(d), a very broad red 'stripe' lies in the middle, inside which we expected to lock an approximate solution.

Referring to figure 4.8(d), we conducted experiments, and obtained results as shown in figure 4.8(e). We scanned this 'map' with a resolution of 0.0025 mm (including 21×21 points), which was 1/4 of that in figure 4.8(c). The experimental results of figure 4.8(e) agreed well with figure 4.8(d).

Based on measured results of figure 4.8(e), we fixed the optimal combination of two thicknesses at point M_3, with a high resolution of 0.0025 mm. At M_3, the peak intensity reached up to 0.996, approaching the target the most in figure 4.8(e). Again, the optimal position M_3 was located inside the red broad 'stripe'.

We also roughly verified our estimation that the peak intensity at M_3 was

the maximum by plotting peak intensities along two axes (x_a–x_b, blue dots; y_a–y_b, orange dots) of point M_3, shown as the plot next to figure 4.8(e). We could confirm that the highest peak intensity along either axis emerged at the intersection, M_3.

Figure 4.8(f) shows the distributions of spectral phases at three different conditions. The same as in the case of five Raman components, M_1 (black) was the initial point before the process of MP, where we started numerical exploration. M_2 (blue) was a point with low peak intensity and far from the optimum, which we regarded as a reference. And M_3 (red) was the optimal point we determined experimentally. By contrast, spectral phases at both M_1 and M_2 varied widely and were far from the optimum; while spectral phases at M_3 were very close to zero rad. Pink line is a linear fitting of spectral phases at M_3. Again, at the optimal point, M_3, nearly linear distribution of spectral phases (close to zero rad) were achieved, with which we were able to reconstruct ultrafast pulses near Fourier transform limited condition. Spectral phases after subtracting linear relation at point M_3 were: Ω_{-2}, - 0.048; Ω_{-1}, 0.083; Ω_0, - 0.032; Ω_1, - 0.048; Ω_2, 0.101; Ω_3, -0.056 (rad).

Here, for phase manipulation of six Raman components, through numerically exploring and experimentally verifying the distributions of peak intensities as functions of two thicknesses two times, we were finally able to lock the optimal point, M_3, which approached the target of phase distribution the most.

Also refer to chapter 5 for the discussions of precision during the process of phase manipulation.

4.3.3 Results of phase manipulation of seven Raman components

Succeeding in manipulating spectral phases of five and six Raman components, we expected to expand the spectrum of MP to seven Raman components (2,403–343 nm). Ω_4 (343 nm) is in the ultraviolet region, therefore, by far we have expanded the spectrum, for both MA and MP, to mid-infrared, visible,

and ultraviolet region (2,403–343 nm).

Figure 4.9 shows main results of phase manipulation of seven Raman components.

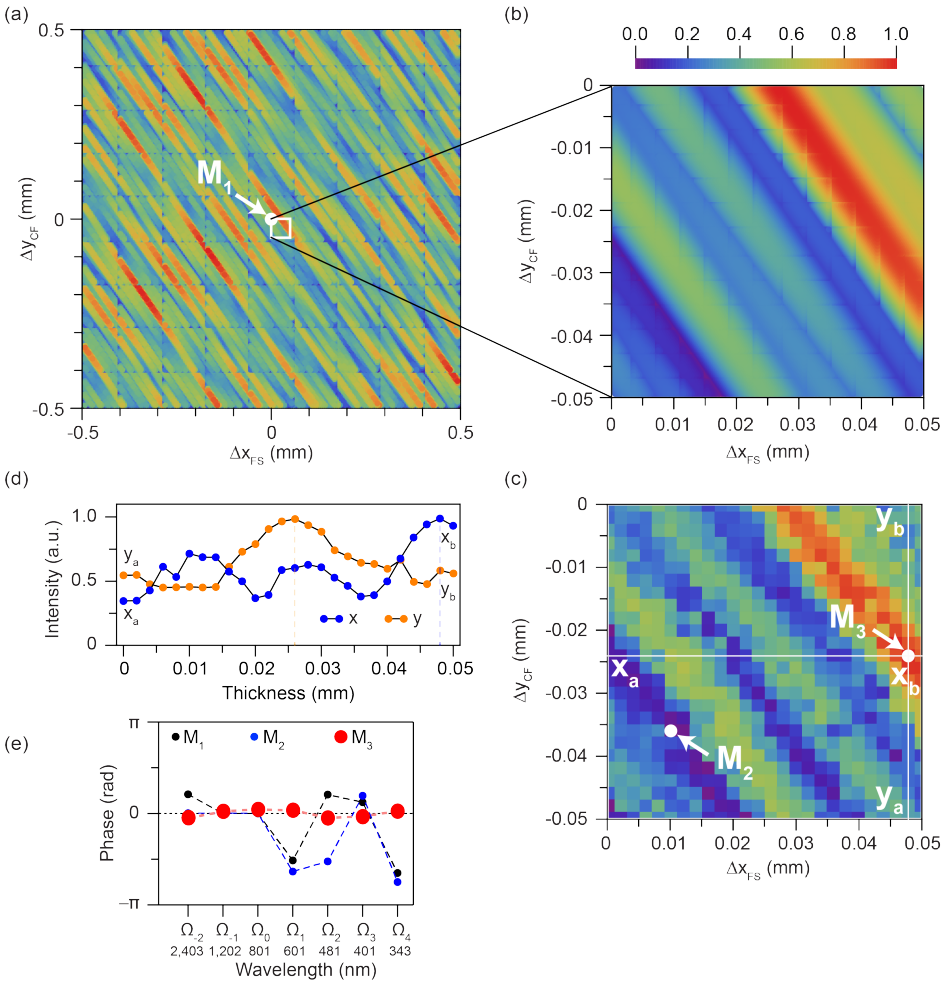

Figure 4.9: Results of phase manipulation of seven Raman components. (a), Calculated 2D plot of peak values of electric field intensity waveforms as functions of fused silica (Δx_{FS}) and calcium fluoride (Δy_{CF}) thicknesses within a range of 1×1 mm^2. White rectangle indicates the maximal size of an area to be verified in experiment. Point M_1 indicates the initial condition determined experimentally. (b), Enlarged 2D plot of the range (0.05×0.05 mm^2) indicated by the white rectangle in (a). (c), 2D plot of observed peak values of electric field intensity waveforms, in which we explored the area corresponding to that in (b) with a resolution of 0.002 mm and 26×26 points. Point M_2 indicates a reference point which has a low peak intensity and is far from the optimum. Point M_3 indicates an optimal point determined experimentally. (d), Plot of distributions of peak intensities along x_a–x_b (blue dots) and y_a–y_b (orange dots) axes of M_3, respectively.

Figure 4.9: (Previous page.) **e**, Spectral phases observed at positions M_1 (initial position, black), M_2 (weak position, blue), and M_3 (optimal position, red), respectively. Pink line (least square fit) shows linear fitting of spectral phases at M_3.

In a similar manner to phase manipulation on five and six Raman components, by moving delay stage on the arm of reference to sweep delay time τ, we acquired the first raw data of intensity oscillations of six interfered SFG components. In this scanning, we again moved delay stage in 100 steps, with each step moving 0.036 μm to obtain three periods of sinusoidal intensity oscillations of all interfered SFG components.

Then we fit the first raw data with sinusoidal functions for all six intensity oscillations of SFG components. In this process, we extracted six SFG phases of the first raw data, which are (confined within -π–+π) Ω_1, 2.518; Ω_2, 1.860; Ω_3, -2.810; Ω_4, -0.403; Ω_5, -1.991; and Ω_6, 1.150 (rad), respectively. Standard errors of fitting of raw data are the same as the cases of five and six Raman components, which were due to intensity fluctuations in Raman process.

Then we retrieved spectral phases of seven fundamental RCs (confined to -π–+π): Ω_{-2}, 0.658; Ω_{-1}, 0; Ω_0, 0; Ω_1, -1.613; Ω_2, 0.649; Ω_3, 0.387; and Ω_4, -2.045 (rad), respectively.

According to retrieved fundamental phases, we calculated the normalized intensity of the initial point as 0.463 (shown as M_1 in figure 4.9(a)). Then we adjusted two thicknesses to calculate and predict how the peak intensities would change over a wide area, 1×1 mm^2 in figure 4.9(a).

However, as the spectrum to be handled broadened, the difficulty of phase manipulation increased, in terms of requirement of finer resolution. Compared to six Raman components, for the same size of intensity 'map', we had to raise the resolution of adjustment of two thicknesses in the case of seven for fixing the optimum. This meant that more time was consumed and more careful determination of experimental implementation was required when coping with seven RCs. Refer to chapter 5 for relevant discussions.

Understanding the difficulty of manipulating spectral phases of seven RCs,

we paid more attention to selecting the appropriate small area to experimentally execute, and scanning such area with very suitable resolution.

White frame in figure 4.9(a) indicates a vastly reduced area of distribution of peak intensities, which we determined to scan in experiment. Figure 4.9(b) is an enlarged view of the white frame in figure 4.9(a), which is 0.05×0.05 mm^2, only 1/400 of the size of figure 4.9(a). In this 'map' of peak intensities, we could also see a red wide 'stripe', inside which we expected to find an approximate solution.

Referring to figure 4.9(b), we conducted experiments with a resolution of 0.002 mm and 26×26 points. The experimental results are shown in figure 4.9(c). Obviously, again we acquired experimental results that were consistent with numerical calculation. Based on experimental results in figure 4.9(c), we determined an optimal combination of two thicknesses at point M_3, with a very high resolution of 0.002 mm. Also the optimal position, M_3 was located inside the red broad 'stripe'.

We could also roughly verify our estimation that the peak intensity at point M_3 was the maximum by plotting peak intensities along two axes of M_3. Figure 4.9(d) shows distributions of peak intensities along x_a–x_b (blue dots) and y_a–y_b (orange dots) axes of point M_3. We confirmed that the highest peak intensity along either axis emerged at the intersection, M_3.

Figure 4.9(e) shows distributions of spectral phases at three representative conditions. Similar to the case of five or six Raman components, M_1 (black) was the initial point before the process of MP, where we started numerical exploration. M_2 (blue) was a point with low peak intensity and far from the optimum, which we regarded as a reference. And M_3 (red) was the optimal point we determined experimentally. By contrast, spectral phases at both points of M_1 and M_2 were distributed over a wide range and far from zero rad; while spectral phases at M_3 were the 'flattest' at zero rad of the three points. Pink line is a linear fitting of spectral phases at M_3. Again, at the optimal point M_3, nearly linear distribution of spectral phases (close to zero rad) was achieved, with which we were able to construct ultrafast pulses near Fourier transform limited condition. Spectral phases after subtracting linear relation at point

M_3 were: Ω_{-2}, - 0.141; Ω_{-1}, 0.073; Ω_0, 0.139; Ω_1, 0.112; Ω_2, - 0.154; Ω_3, -0.109; Ω_4, 0.079 (rad).

Here, for phase manipulation on seven Raman components, through numerically exploring and experimentally verifying the 'map' of intensity distribution once, we locked the optimal point M_3, which approached the target of phase distribution the most in figure 4.9(c). The reason why we needed fewer times of scanning intensity map than for the case of six RCs was that, although the resolution needed and the difficulty of phase retrieval for seven RCs were far higher than for the cases of five and six RCs, we prudently selected an appropriate area with high intensities included and experimentally implemented it with very fine resolution, in which process we made use of the feasibility and reliability of our method of MP obtained from experiments with both five and six RCs.

So far, we succeeded in manipulating spectral phases of five, six, and seven Raman components (covering mid-infrared, visible, and ultraviolet wavelength range) by using the same device and procedures. In fact, our device of phase manipulation has the capability of manipulating a rather broad bandwidth (about 1 PHz, over 12 high-order Raman components), expanding from mid infrared to deep ultraviolet with an accuracy comparable to the above cases.

4.4 Electric field intensity waveforms

To further make use of the results of both amplitude and phase manipulations, we could characterize electric field intensity waveforms of the spectrum of Raman components in the time domain according to Fourier transformation. In that sense, we could achieve ultrafast pulses of different durations by probing different number of Raman components.

Following the way of introducing results of MA and MP, I will first present ultrafast pulses achieved by controlling five Raman components (RCs), then move to the case of six RCs, and finally to the case of seven RCs. As a prediction or prospect, I will also incorporate the pulses calculated with eight Raman

components at Fourier transform limited (TL) condition.

4.4.1 Electric field intensity waveforms achieved with five Raman components

Figure 4.10 shows electric field intensity waveforms reconstructed with achieved amplitudes and spectral phases of five high-order Raman components (spanning Ω_{-2} to Ω_2) at different conditions.

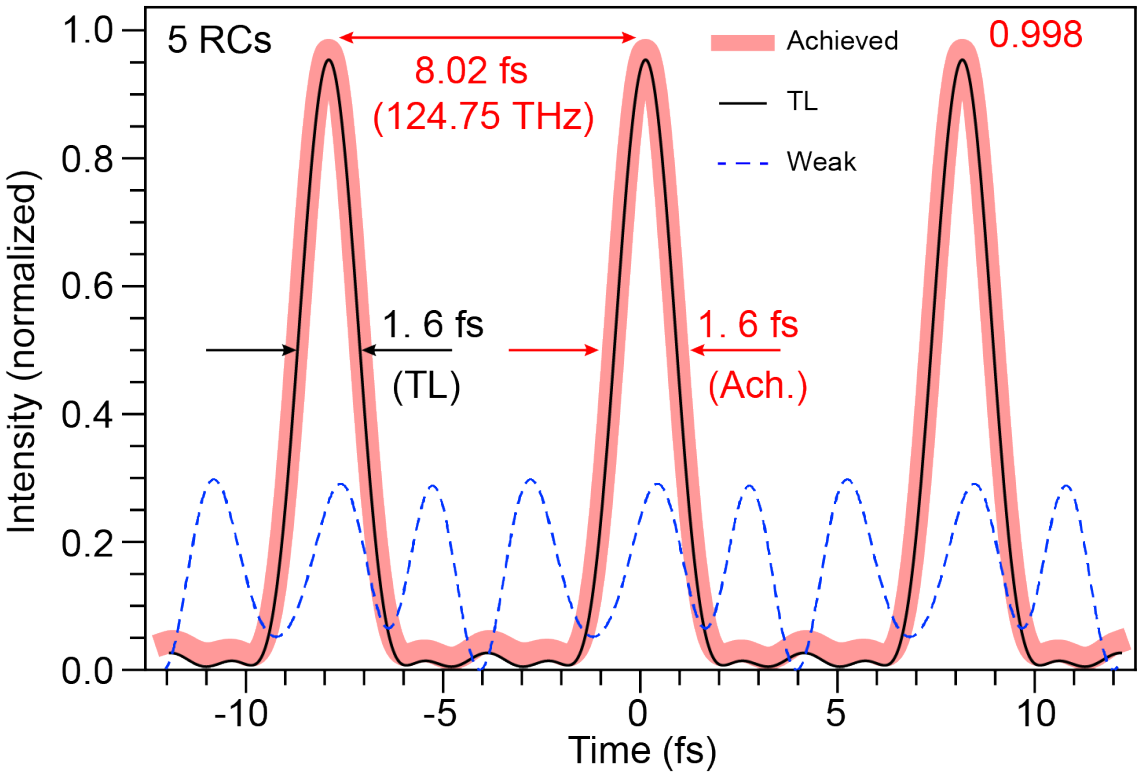

Figure 4.10: Retrieved electric field intensity waveforms of five high-order Raman components (spanning Ω_{-2} to Ω_2) at different conditions. Thick pink, thin black, and dashed blue lines indicate electric field intensity waveforms achieved at optimal point (M_3), Fourier transform limited condition, and reference point (M_2), respectively. The pulse duration (pink) of achieved electric field intensity waveforms at full width at half maximum (FWHM) is 1.6 fs, with a repetition period of 8.02 fs (relating to frequency space of 125 THz) and a peak intensity of 0.998, very close to TL condition.

As shown in figure 4.10, based on retrieved spectral phases with manipulated amplitudes, we were able to reconstruct electric field intensity waveforms of such spectrum of Raman components in the time domain according to Fourier transformation (see equation 2.27).

Pink thick line shows electric field intensity waveforms achieved at the optimal point, M_3. It was a train of ultrafast pulses, with a repetition period of 8.02 fs (or 125 THz). Pulse duration at full width at half maximum (FWHM) was 1.6 fs. The pulse duration achieved at point M_3 was equal to that calculated at Fourier transform limited condition (black solid line)–all spectral phases of fundamental RCs were exactly zero rad. The peak intensity achieved at the optimal point was 0.998, comparing against normalized peak intensity at the TL condition (i.e., unity) [88].

Dotted blue line is electric field intensity waveforms reconstructed at the reference point, M_2, which had a low peak intensity of 0.359 (also refer to figure 4.6(c)). Through the process of phase manipulation, we could see that the electric field intensity waveforms have been improved substantially, from a shape like a noise burst, to a train of ultrafast pulses close to Fourier transform limited condition.

We also evaluated the precision of achieved pulse train, because they were reconstructed with achieved spectral phases and thus constrained by their precision of fitting in equation 2.26. Such difference (due to retrieval of spectral phases) was estimated to be about 0.001 fs (i.e., 1.6354 fs $\rightarrow$ 1.6461 fs if in detail) at the optimal point M_3. Such evaluation meant that the difference caused by the precision of fitting of phases of interfered SFG components was negligible.

4.4.2 Electric field intensity waveforms achieved with six Raman components

Figure 4.11 shows electric field intensity waveforms reconstructed according to achieved amplitudes and phases of six high-order Raman components (spanning Ω_{-2} to Ω_3) at different conditions.

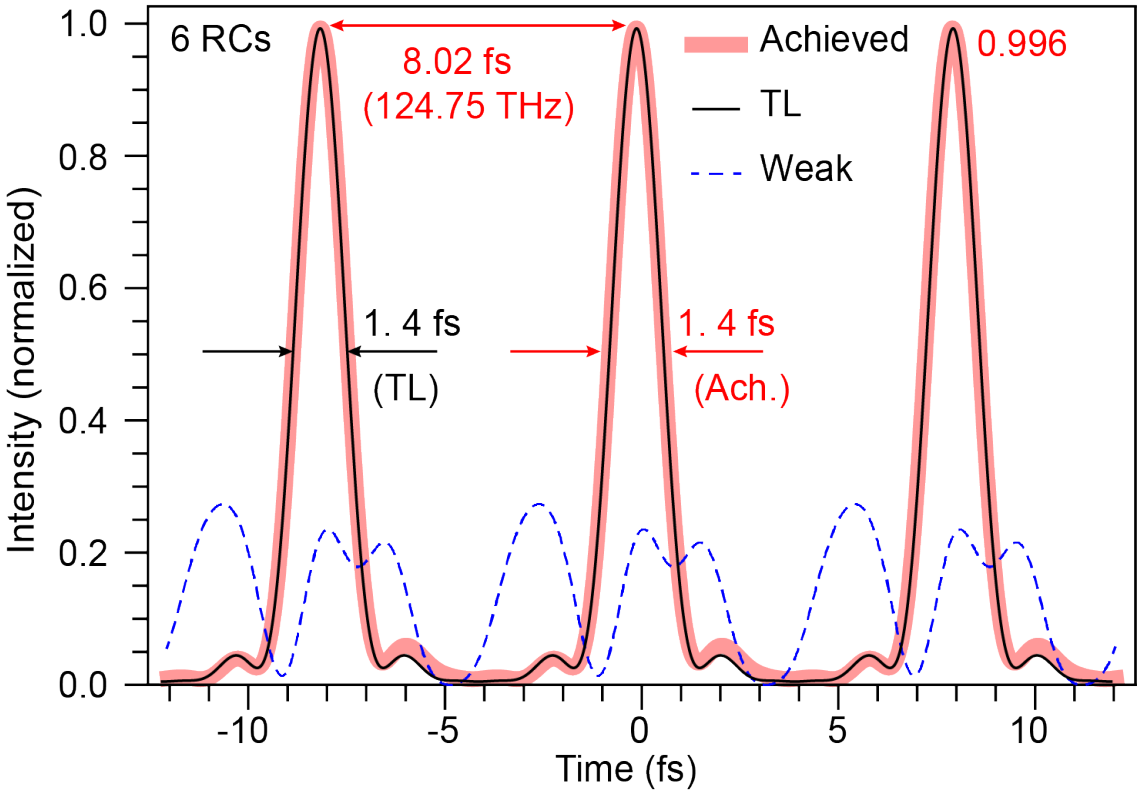

Figure 4.11: Retrieved electric field intensity waveforms of six high-order Raman components (spanning Ω_{-2} to Ω_3) at different conditions. Thick pink, thin black, and dashed blue lines indicate electric field intensity waveforms achieved at optimal point (M_3), TL condition, and reference point (M_2), respectively. The pulse duration (pink) achieved at point M_3 at FWHM is 1.4 fs, with a repetition period of 8.02 fs and a peak intensity of 0.996, close to TL condition.

In figure 4.11, pink thick line shows electric field intensity waveforms reconstructed with achieved amplitudes and phases at the optimal point M_3. It had a repetition period of 8.02 fs (or 125 THz). The pulse duration at FWHM was 1.4 fs, which was equal to that at TL condition (black solid line). The peak intensity at M_3 was 0.996, comparing against normalized intensity at TL condition.

Dotted blue line is electric field intensity waveforms reconstructed at reference point, M_2, which had a peak intensity of 0.353 (refer to figure 4.8(c)). Through the process of phase manipulation, we also improved the pulses of six

Raman components drastically from a shape like a noise burst to an ultrafast pulse train near TL condition.

We also evaluated the achieved pulse train of six Raman components by considering the precision of fitting of phases of interfered SFG components. Such difference was estimated to be about 0.003 fs (i.e., 1.3836 fs $\rightarrow$ 1.3869 fs if in detail) at the optimal point, M_3, which was also negligible.

4.4.3 Electric field intensity waveforms achieved with seven Raman components

Figure 4.12 shows electric field intensity waveforms reconstructed with achieved amplitudes and phases of seven high-order Raman components (spanning Ω_{-2} to Ω_4) at different conditions.

In figure 4.12, pink thick line shows electric field intensity waveforms reconstructed at optimal point (M_3). This train of pulses had a repetition period of 8.02 fs (or 125 THz). The pulse duration achieved at M_3 at FWHM was 1.2 fs, which was equal to that at TL condition (black solid line). The peak value of achieved e-field intensity waveforms at M_3 was 0.988, comparing against unity at TL condition.

Dotted blue line is electric field intensity waveforms reconstructed at reference point, M_2, which had a low peak intensity of 0.312 (refer to figure 4.9(c)). From the point M_2–through the process of phase manipulation–to M_3, we again improved the shape of electric field intensity waveforms drastically and achieved a train of ultrafast pulses near TL condition.

In the case of seven Raman components, the difference of pulse duration of electric field intensity waveforms due to the precision of fitting of spectral phases was estimated to be 0.004 fs (i.e., 1.220 fs $\rightarrow$ 1.224 fs if in detail) at the optimal point, M_3, still negligible.

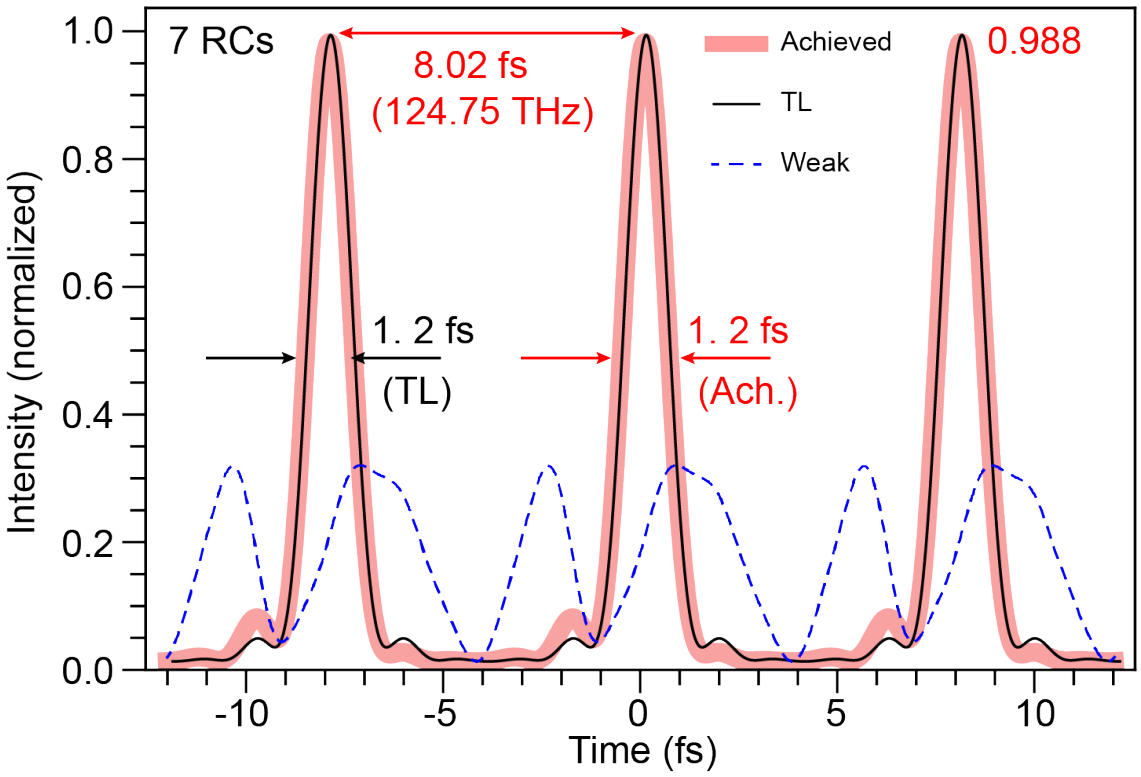

Figure 4.12: Retrieved electric field intensity waveforms of seven high-order Raman components (spanning Ω_{-2} to Ω_4) at different conditions. Thick pink, thin black, and dashed blue lines indicate electric field intensity waveforms achieved at optimal point (M_3), TL condition, and reference point (M_2), respectively. The pulse duration (pink) achieved at M_3 at FWHM is 1.2 fs, with a repetition period of 8.02 fs and a peak intensity of 0.988, near TL condition.

We can see that as the spectrum of Raman components expanded, the width (FWHM) of electric field intensity waveforms decreased. That is, when targeting synthesizing ultrafast optical pulses, the pulse duration is determined by the bandwidth of the spectrum, i.e., the number of high-order Raman components.

The current situation is that we have been able to manipulate amplitudes and phases of up to seven high-order Raman components–a spectrum spanning Ω_{-2} to Ω_4 (2,403–343 nm), and reconstructed a train of 1.2 fs ultrafast pulses in the time domain.

Note that millions of 1 femtosecond pulses were formed under the pulse envelope of the driving lasers, which had an envelope duration of about 7 ns.

4.4.4 Electric field intensity waveforms predicted with eight Raman components

Figure 4.13 shows electric field intensity waveforms predicted with eight high-order Raman components (spanning Ω_{-2} to Ω_5), which were calculated at Fourier transform limited condition.

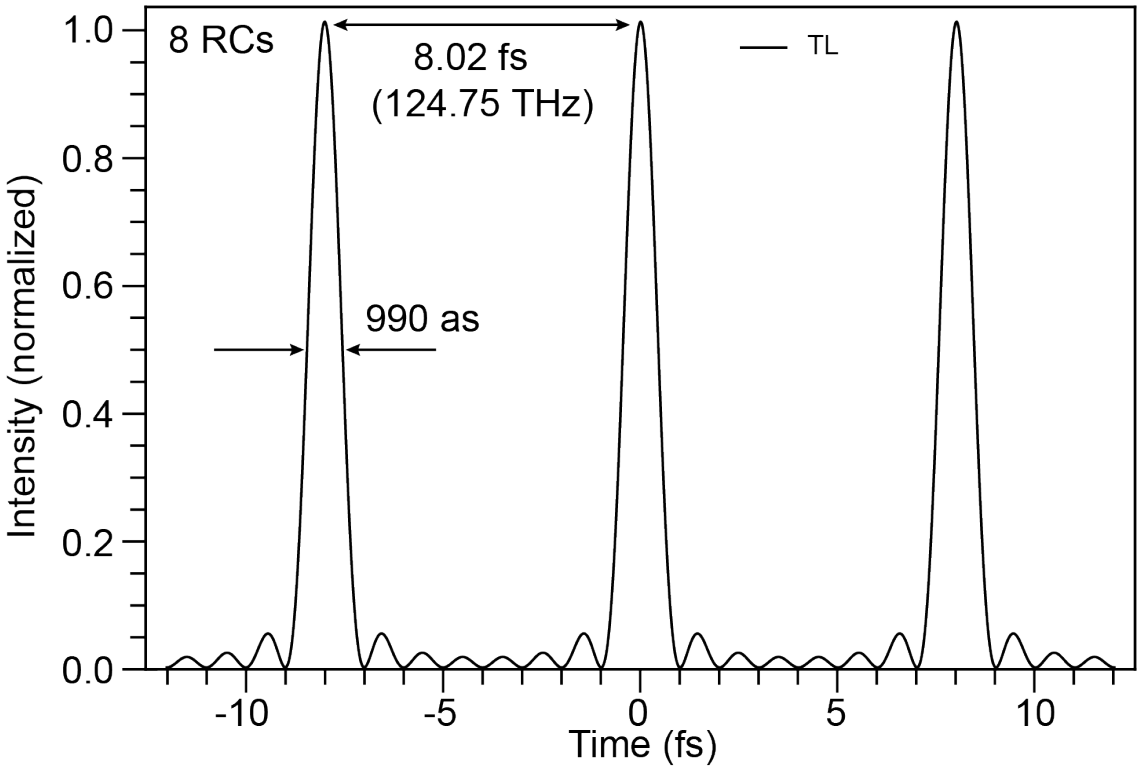

Figure 4.13: Calculated electric field intensity waveforms of eight high-order Raman components (spanning Ω_{-2} to Ω_5) at TL condition. The pulse duration (thin black line) calculated at FWHM is 990 as, with a repetition period of 8.02 fs and a peak intensity of unity.

As shown in figure 4.13, we calculated electric field intensity waveforms of eight Raman components, by assuming that all eight components had the

same phase–zero rad, and adding an appropriate amplitude of 300 nm to the achieved amplitude distribution of seven components. Apparently, if we were able to handle eight Raman components in experiment, in a similar manner to what we did with five, six, and seven, we could expect to achieve a train of attosecond pulses (990 as) near TL condition.

Bibliography of Chapter 4

[83] A. V. Sokolov et al. “Raman generation by phased and antiphased molecular states”. In: *Phys. Rev. Lett.* 85 (2000), pp. 562–565.

[84] J. Q. Liang et al. “Sideband generation using strongly driven Raman coherence in solid hydrogen”. In: *Phys. Rev. Lett.* 85 (2000), pp. 2474–2477.

[85] A. V. Sokolov et al. “Generation and control of femtosecond pulses by molecular modulation”. In: *J. of Mod. Opt.* 52 (2005), pp. 285–304.

[86] T. Suzuki, M. Hirai, and M. Katsuragawa. “Octave-spanning Raman comb with carrier envelope offset control”. In: *Phys. Rev. Lett.* 101 (2008), p. 243602.

[87] S. Baker et al. “Femtosecond to attosecond light pulses from a molecular modulator”. In: *Nat. Photon.* 5 (2011), pp. 664–671.

[88] P. Lazaridis, G. Debarge, and P. Gallion. “Time-bandwidth product of chirped sech^2 pulses: application to phase-amplitude-coupling factor measurement”. In: *Opt. Lett.* 20 (1995), pp. 1160–1162.

Chapter 5

Discussions

In this chapter, I will discuss prominent issues we faced during experiments. I classified them into three sections, following cases introduced in the former chapter.

5.1 Discussions in amplitude manipulation

What are differences of manipulating amplitudes of five, six, and seven Raman components?

In brief, escalation of the number of Raman components increases difficulty of manipulating amplitudes.

On one hand, with increment of Raman components, we had to set the target more prudently. Because within limited exploring range (i.e., limited translation range of thickness of CQ pair–about 20 mm in total), we could not approach whatever target we set; otherwise, we had to enormously extend adjustment range of thickness. This is why we did not obtain exactly 'flat' distribution of amplitudes in results of amplitude manipulation but near 'flat', which still made sense when reconstructing ultrafast pulses.

On the other hand, with more Raman components, the difficulty of numer-

ically exploring the optimal thickness also rose. That is, when manipulating five Raman components, we could easily approach the target by finding optimum within a very short range. However, when raising the number of Raman components to six, and even seven, we had to search a much wider range to find an approximate solution to the target. We could judge from optimal thicknesses explored with different number of Raman components: -0.7996 mm with five Raman components; -0.8256 mm with six Raman components; and 4.7947 mm with seven Raman components.

In addition, we manipulated amplitudes of five, six, and seven Raman components on different days, and thus they each had somewhat different preconditions of Raman scattering. Refer to original powers of different number of Raman components before MA in chapter 4.

How did we set target powers?

In principle, we are able to arbitrarily manipulate amplitudes (and thus powers) of highly discrete spectra. However, due to two reasons, we set our target powers as shown in chapter 4. First, our aim through manipulating amplitudes is to generate ultrashort pulses in the time domain; therefore, ideally, we want to make all the amplitudes distribute at the same value–flat amplitude distribution. Second, the original powers of our Raman components are widely distributed, from several kW to several hundreds of kW; therefore, we would like to set the target with such features: keep the weak power of 2.4 μm at maximum while maintain other powers as high as possible. Considering these two reasons, we set the near flat target powers as exhibited in chapter 4.

Precision of fitting lines according to initial scanning

As evaluation of precision of fitting lines for different number of Raman components remained the same, I here only show the estimation of seven Raman components (RCs), which also covered the cases of five, and six RCs.

According to equation 2.2, I used a function model of fitting given as $y = A0 + B0 \times \sin(2\pi x/C0 + D0)$. The precision of fitting functions was estimated in table 5.1.

Item	2,403 nm	1,202 nm	801 nm	601 nm	481 nm	400 nm	343 nm
A0	4.70	256.14	70.91	21.73	16.05	8.05	3.49
A0 SE	0.0075	0.18	0.026	0.029	0.0092	0.0072	0.0044
B0	4.59	-251.40	-67.74	20.46	-15.40	-7.56	3.21
B0 SE	0.011	0.23	0.036	0.040	0.013	0.010	0.0062
C0	1.18	0.53	0.35	0.25	0.20	0.16	0.13
C0 SE	4.88E-4	1.21E-4	2.92E-5	6.23E-5	1.55E-5	1.60E-5	1.59E-5
D0	0.51	1.58	1.66	0.77	1.72	0.29	3.06
D0 SE	0.0048	0.0019	0.0011	0.0042	0.0017	0.0027	0.0039

Table 5.1: Precision of fitting lines of initial scanning in MA. SE: standard errors of fitting parameters; "E" corresponds to "power of 10", i.e., "E-4" stands for "10^{-4}", etc. Note that C0 in the model of fitting represents period.

As shown in table 5.1, standard errors of different parameters in the fitting functions were very small. Especially, parameter C0, which corresponds to periods of power oscillations of different Raman components, maintains standard errors of 10^{-4} at the most. Therefore, the fitting lines were reliable.

In addition, I also made a comparison of periods of power oscillations between experimental results and theoretical calculation. Theoretical values were calculated according to Sellmeier equation of crystal quartz [89] on different wavelengths. See table 5.2 for the comparison. Experimental results were actually in good agreement with theoretical calculation.

Item	2,403 nm	1,202 nm	801 nm	601 nm	481 nm	400 nm	343 nm
Theoretical periods (mm)	1.28	0.55	0.35	0.26	0.20	0.16	0.13
Experimental periods (mm)	1.18	0.53	0.35	0.25	0.20	0.16	0.13
Difference	0.10	0.016	0.0084	0.0061	0.0039	0.0016	-0.0016
Difference ratio (%)	7.86	2.86	2.37	2.33	1.95	0.97	-1.20

Table 5.2: Comparison of periods of power oscillations between experimental results and theoretical calculation. Difference = theoretical - experimental; difference ratio = difference / theoretical.

Precision of achieved power distribution

Since we manipulated amplitudes of different number of Raman components on different days (thus with different preconditions of Raman generation), the differences between achieved results and the target were somewhat different for the cases of five, six, and seven Raman components. But the levels of such differences stayed the same. Here I list out the precision of achieved power distribution of seven Raman components.

Table 5.3 shows differences among target, numerical exploration, and achieved results. The energy meter (Ophir Nova 2) we used for measuring energies had an uncertainty of about $\pm 2.5\%$, for an averaged measuring time of 30 seconds.

Item	2,403 nm	1,202 nm	801 nm	601 nm	481 nm	400 nm	343 nm
Target (kW)	8.57	5.00	18.57	25.71	11.43	14.29	5.71
Exploration (kW)	8.53	4.77	18.75	26.17	11.71	13.91	5.64
Difference TE (kW)	0.046	0.23	-0.18	-0.46	-0.28	0.38	0.07
Difference TE ratio (%)	0.53	4.63	-0.96	-1.79	-2.46	2.64	1.25
Achieved (kW)	8.71	4.14	16.29	27.29	9.00	13.57	5.43
Difference TA (kW)	-0.14	0.86	2.29	-1.57	2.43	0.71	0.29
Difference TA ratio (%)	-1.67	17.14	12.31	-6.11	21.25	5.00	5.00

Table 5.3: Precision of achieved power distribution of MA, for the case of seven RCs. Difference TE=target-exploration; difference TE ratio = difference TE / target; difference TA = target - achieved; difference TA ratio = difference TA / target.

In table 5.3, we can see that the power distribution of numerical exploration at the optimal thickness (4.7947 mm) is very close to that of the target, and the maximal difference ratio is 4.63%. However, as for the achieved power distribution, the maximal difference ratio is 21.25%. Hereby, we have to recall that both Raman scattering and the energy meter have their 'fluctuations'– up to 10% at most. At such precision of achieved powers, the results of MA are still suitable for subsequent experiments (i.e., manipulating phases and constructing pulses).

How much does the precision of achieved power distribution affect ultrashort pulses?

Since there existed differences between achieved power distribution and the target, we had to evaluate its influence to reconstructing ultrafast pulses.

To make it easy, I assume that all spectral phases are zero rad. The pulse duration (at FWHM) of the target, and achieved power distribution are 1.135

fs, and 1.131 fs, respectively. That is, the pulse width only has a small amount of change–0.004 fs–due to differences between the target and achieved power distribution. Note that the above pulse durations are different from relevant results in chapter 4, because the power distributions were slightly different on two different days (of MA and MP).

In a few words, the differences between achieved results and the target make little contribution to the pulse duration of reconstructed electric field intensity waveforms.

Discussions on power distribution before and after MA

Here we may be concerned about how much power of every component remains during the process of sweeping thickness of crystal quartz, and what are the ratios between before and after MA. The table below shows such discussions for the case of seven RCs.

Item	2,403 nm	1,202 nm	801 nm	601 nm	481 nm	400 nm	343 nm
Maximum (kW)	9.3	507.5	138.7	42.2	31.5	15.6	6.7
Minimum (kW)	0.1	4.7	3.2	1.3	0.7	0.5	0.3
Ratio IA (%)	1.2	0.9	2.3	3.0	2.1	3.2	4.1
Before MA (kW)	12.0	692.9	215.0	69.6	47.1	24.6	11.1
After MA (kW)	8.7	4.1	16.3	27.3	9.0	13.6	5.4
Ratio AB (%)	72.6	0.6	7.6	39.2	19.1	55.2	48.7

Table 5.4: Comparison of different powers, for the case of seven RCs. Maximum, maximal value of power oscillation as a function of thickness of crystal quartz (CQ); Minimum, minimal value of power oscillation as a function of thickness of CQ; Ratio IA = Minimum / Maximum; Before MA, original power distribution before MA; After MA, achieved power distribution at optimal thickness of crystal quartz; Ratio AB = After MA / Before MA.

From the above table, we find that the remaining powers (minimum) of power oscillation as a function of CQ thickness are very small portion. Through

the process of MA, we have largely suppressed powers of Raman components in the middle while reserving those on the two sides.

5.2 Discussions in phase manipulation

What are the differences between manipulating phases of five, six, and seven Raman components?

Escalation of the number of Raman components during the process of manipulating phases raises experimental resolution of distribution of peak intensities when exploring the optimum.

For manipulating the phases of five RCs, we numerically explored and experimentally verified a 'map' of peak intensities, having an area of 0.4×0.3 mm^2 with a resolution of 0.01 mm, including 41×31 points. With such a rough resolution, we scanned the 'map' only once and were able to lock an optimal position. Moreover, the optimum had a peak intensity of 0.998, very close to Fourier transform limited condition.

However, with six Raman components, we had to scan the map two times with step-wise increased resolution for locking the optimum. In detail, we first selected and scanned an intensity 'map' of 0.2×0.2 mm^2 with a rough resolution of 0.01 mm, making 21×21 points. This map confirmed reliability of numerical exploration. However, inside this still-large area, we could not lock an optimal position with high accuracy. In the next step, we focused on a 'map' of 0.05×0.05 mm^2 with a high resolution of 0.0025 mm, making 21×21 points. The resolution in the second 'map' enabled us to settle an optimal position, M_3, which was an approximate solution to the phase distribution of target. The peak intensity at such optimal point reached 0.996, close to TL condition, although it declined a bit comparing to that of five RCs.

As the number of Raman components rose to seven, despite that we experimentally scanned the 'map' of peak intensities only once, it had an area of merely 0.05×0.05 mm^2 with a superb resolution of 0.002 mm, making 26×26 points. The reason why we scanned the 'map' only once is the following. In

experiment of manipulating phases, confined by the angles of phase matching of 10 μm thick BBO crystal (on such a broadband spectrum), we had to measure phases of six interfered SFG components separately and spend far more time building up the 'map' of peak intensities (i.e., figure 4.9(c)). Fortunately, based on the confirmation of correctness of numerical exploration on five and six RCs, we could carefully select a 'map' with an area of high peak intensities included, and experimentally execute it with a very high resolution of 0.002 mm. Eventually, electric field intensity waveforms reconstructed at the optimal point had a peak intensity of 0.988, still near TL condition, but it downgraded somehow comparing to the cases of five and six RCs.

Comparing intensity 'maps' (experimentally obtained) of different number of Raman components, for locking the optimum, the resolution was upgraded from 0.01 mm (five RCs) to 0.0025 mm (six RCs), and finally to 0.002 mm (seven RCs). With experimental resolution increased following the increment of Raman components, we actually reduced the size of intensity 'maps' to scan in experiment, in order to quickly approach the optimum,.

How did we select dispersive materials?

In our case, it is allowable to use a single dispersive material to manipulate phases. However, it is difficult to frequently find near optimal solutions when we use one material. That is, we have to adjust thickness of the single material over a wide range to explore a position that corresponds to high peak intensity. However, with two different dispersive materials, we have more freedom to control phases, and can find near optimum more frequently.

In general, we could use transparent dispersive materials that are normally used, such as glass (BK7), fused silica, calcium fluoride, etc. Taking into account transmitting range of wavelengths, we simply selected two common materials, i.e., fused silica and calcium fluoride. Fused silica and calcium fluoride have different refractive indices for the same wavelength, thus corresponding to different dispersions.

Fitting precision of SFG intensity oscillations

According to equation 2.26, in the process of retrieving interfered SFG phases,

we used a fitting model of $y = A0 + B0 * \sin(2\pi t/T_p + D0)$. Table 5.5 is a series of typical data (a random point in the 'map' of peak intensities of seven RCs), for estimating the precision of fitting lines of intensity oscillations of interfered SFG components.

Item	601 nm	481 nm	400 nm	343 nm	300 nm	267 nm
A0	36.53	36.03	120.04	71.32	17.39	8.88
A0 SE	0.38	0.59	1.29	0.68	0.25	0.19
B0	2.81	22.13	-33.43	22.61	-5.28	-4.03
B0 SE	0.54	0.83	1.82	0.96	0.35	0.26
D0	1.73	14.30	-17.28	21.83	5.45	0.75
D0 SE	0.19	0.038	0.055	0.042	0.066	0.065
D0 SE ratio (%)	11.23	0.26	0.32	0.19	1.22	8.69

Table 5.5: Precision of fitting lines of intensity oscillations of interfered SFG components. SE, standard errors. Note that D0 depicts phases of interfered SFG components retrieved from fitting functions. D0 SE ratio= D0 SE/D0.

As shown in table 5.5, standard errors of different parameters, generally speaking, were very small, including the phases of SFG components. The largest standard error of SFG phase was on 601 nm, which reached about 11% of the estimated phase. This standard error was large because the SFG component, 601 nm was mixed partly from 2,403 nm, which was located in the mid-infrared wavelength range, had a weak intensity, and maintained relatively large fluctuation and dispersion.

Why can we make the assumption that the phases of two fundamental Raman components as 0 rad?

In equation 2.26, we can see that to retrieve spectral phase of any fundamental Raman component through linear relationship, there are always two constants included, ψ^R_{-1} and ψ^R_0, and they can be any constants. In practice,

we put phases of ψ_{-1}^{R} and ψ_{0}^{R} as 0 rad. Besides, ψ_{-1}^{R} and ψ_{0}^{R} have no differences with phases of original Raman components (fundamental), ψ_{-1} and ψ_{0}, after transmitting through dispersive materials, because relative delay has been included in equation 2.26.

How much does the precision of phase retrieval affect pulse duration?

After estimating the precision of phase retrieval, we want to know its impact to the width of reconstructed electric field intensity waveforms.

In the case of five Raman components, the precision of phase retrieval caused a variation of 0.001 fs to the pulse duration, i.e., 1.6354 fs $\rightarrow$ 1.6461 fs. And for six RCs, the precision of phase retrieval brought about a variation of 0.003 fs to the pulse duration, i.e., 1.3836 fs $\rightarrow$ 1.3869 fs. For seven RCs, such a variation was 0.004 fs, i.e., 1.220 fs $\rightarrow$ 1.224 fs.

Overall, the precision of phase retrieval had little impact on the pulse duration of reconstructed electric field intensity waveforms.

Damage threshold of all devices of MA and MP

As mentioned in both **Abstract** and **Introduction**, our devices of manipulating amplitudes and phases were capable of resisting high powers. I here clarify damage threshold of each optical element of those manipulation devices.

Crystal quartz has a damage threshold of over 10 GW/cm^2 (data from PhotoTechnica). Glan laser calcite polarizer has a damage threshold of about 20 GW/cm^2 (data from Thorlabs). Fused silica and calcium fluoride have a damage threshold of about 120 GW/cm^2, and 60 GW/cm^2 [90], respectively. These data are based on characteristics of our pulsed lasers–wavelength of about 1,000 nm, repetition rate of 10 Hz, and envelope duration about 10 ns–which may be slightly different from various data sources.

To put it simply, if we postulate that incident laser is about 1,000 nm (with an envelope duraiton of 10 ns and a repetition rate of 10 Hz), our devices of MA and MP can resist an intensity of at least 10 GW/cm^2.

Limitation of the SPIDER-DS system

We need to declare that there exists a limitation of the SPIDER-DS system: we cannot retrieve spectral phases of eight or more Raman components with current SPIDER-DS system. This restraint is owing to finite acceptance angles of BBO crystal.

Figure 5.1 shows acceptance angles of 10 μm thick BBO crystal on different SFG components. In this diagram, we assume that conversion efficiency is confined in the range of 0.5–1. That is, at the joints (solid squares and circles) of distinct SFG components, phases are exactly matched and conversion efficiency is 1; with line segments stretching to their ends, phases are not matched, and conversion efficiency decreases and moves to 0.5 at the ends.

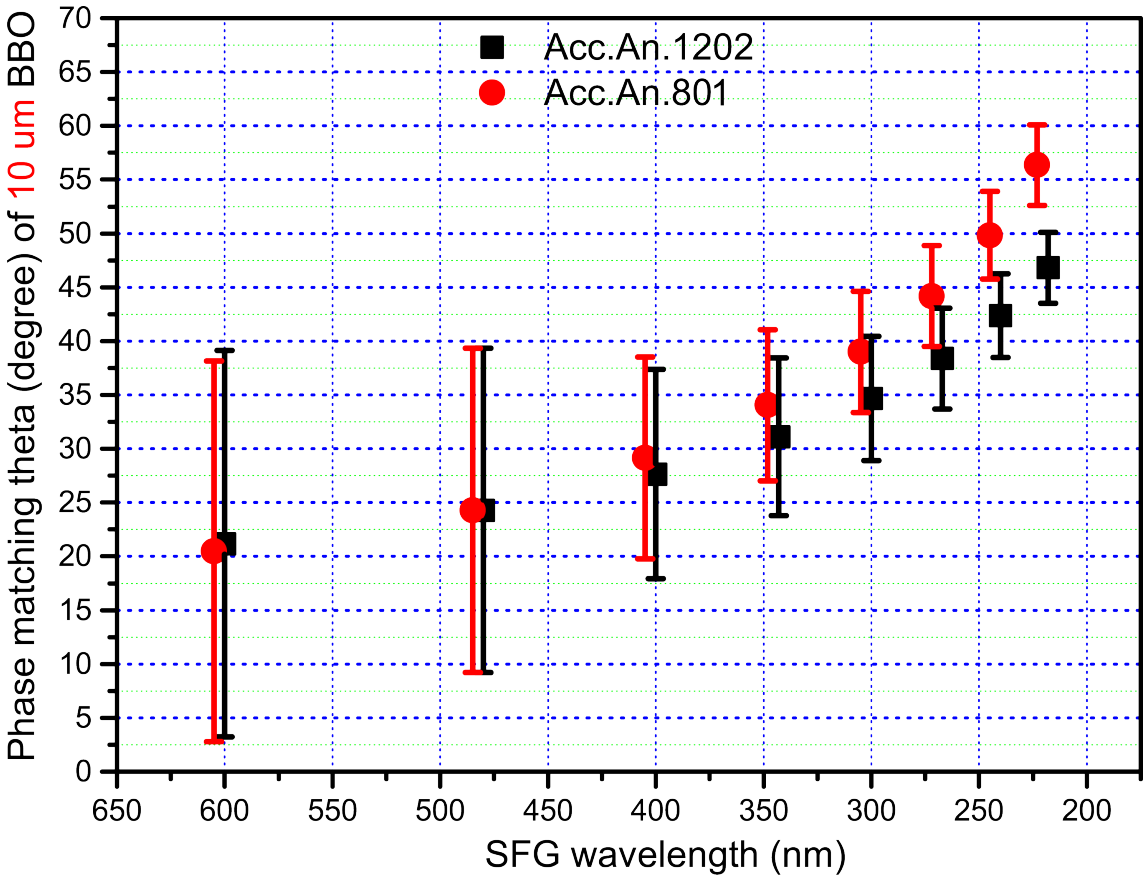

Figure 5.1: Acceptance angles of 10 μm thick BBO crystal. Black line segments represent SFG components derived from 1,202 nm; red line segments represent SFG components derived from 801 nm. Solid squares and circles denote angles where SFG components are phase matched; line segments in between their center and ends denote acceptance angles, where conversion efficiency decreases from 1 to 0.5.

In fact, during experiment of manipulating and measuring spectral phases, we have to choose an appropriate angle of BBO crystal, at which all interfered SFG components (for instance, from 601 nm to 267 nm) should have a conversion efficiency over 0.5, for both branches originating from 1,202 nm and 801 nm. However, as shown in figure 5.1, this requirement can not be satisfied well with 10 μm thick BBO. As acceptance angles drift and depart for different SFG components, we are not able to implement phase retrieval "once and for all" for seven or even more Raman components. Instead, for retrieving phases of seven Raman components, we have to retrieve phases of six interfered SFG

components separately: using two different acceptance angles to retrieve two batches of SFG phases and then combining them together. This is why we spent much more time scanning the 'map' of peak intensities of seven Raman components than for the other two cases.

Furthermore, if expanding the spectrum to eight Raman components, we even have very little chance to find an appropriate acceptance angle for only the highest-order SFG component–240 nm. Because at this wavelength, acceptance angles from either branch are barely overlapping. Hence, we can hardly measure the phases of eight Raman components using the 10 μm thick BBO.

In a word, as a result of limited acceptance angles owing to the thickness of nonlinear optical crystal, there remains a restraint of measuring phases of eight or more Raman components using our SPIDER-DS system.

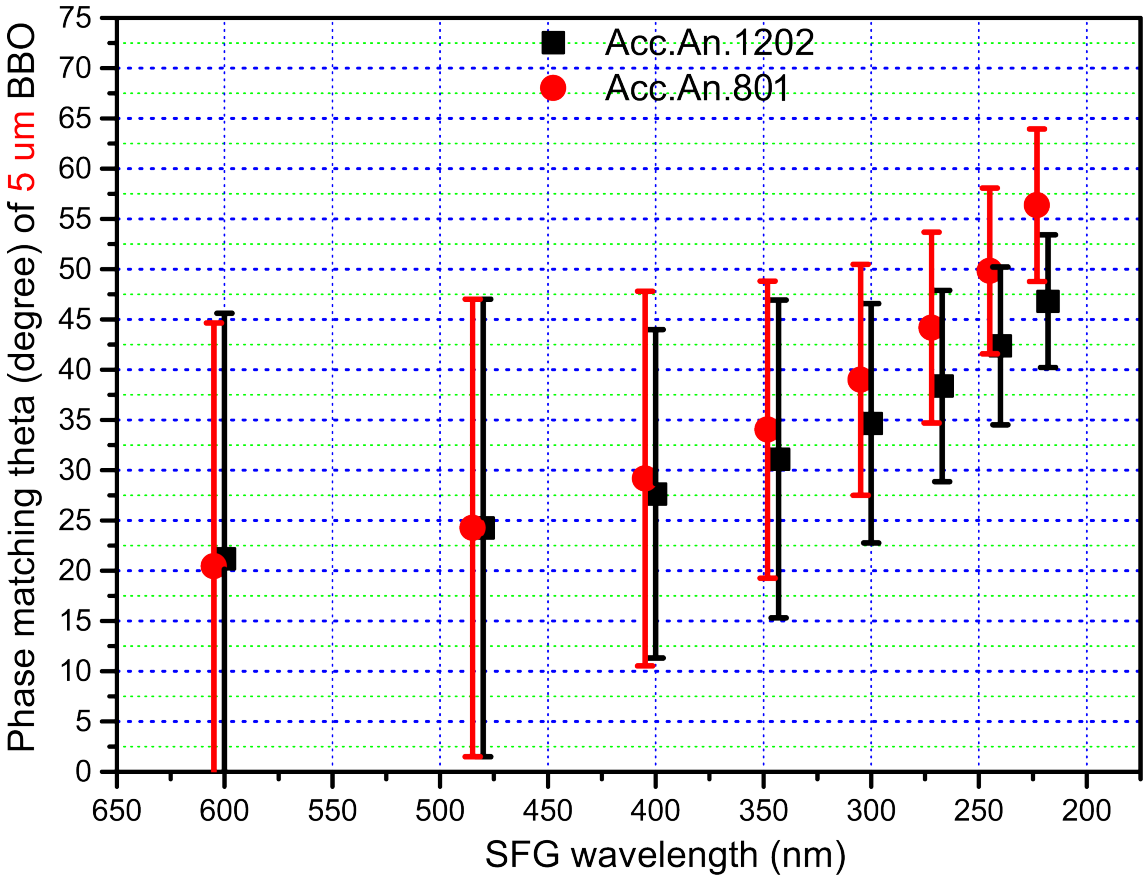

Figure 5.2: Acceptance angles of 5 μm thick BBO crystal. Black line segments represent SFG components derived from 1,202 nm; red line segments represent SFG components derived from 801 nm. Solid squares and circles denote angles where SFG components are phase matched; line segments in between their center and ends denote acceptance angles, where conversion efficiency decreases from 1 to 0.5.

To break the restraint of current SPIDER-DS system, basically, there are possibly three solutions. The first, reduce the thickness of BBO crystal, for example, from 10 μm to 5 μm, which will be discussed later. The second, substitute BBO crystal for other high-efficient nonlinear optical crystals. This work needs more investigation. The third, replace whole SPIDER system for other systems of phase measurement, but generally the problem of limited acceptance angles due to the thickness of nonlinear optical crystals cannot be circumvented.

Figure 5.2 shows acceptance angles of a 5 μm thick BBO crystal. In this case, it is easy to find a suitable angle (around 42 degrees) for simultaneously measuring spectral phases of interfered SFG components from 601 nm to 240 nm. Moreover, it is even available to measure the phase of SFG component up to 218 nm, although again we have to measure the phases of all eight SFG components separately, with two batches.

Limitations of our novel optical technology

So far, we have experimentally manipulated amplitudes and phases of five, six, and seven Raman components in sequence. According to theoretical calculation, our manipulation devices can handle a spectrum with a bandwidth of about 1.4 PHz, including 12 Raman components. And even though we increase the number of waveplate in MA or that of dispersive material in MP, the bandwidth of Raman components we can handle cannot be increased more. However, due to two limitations, we currently could not move forward to handling eight or more Raman components, using our manipulation devices.

1, Low power of high-order Raman components, due to Raman process. The original powers of 300 nm and higher orders were very weak; therefore, we were not able to utilize them to broaden the spectrum that our manipulation devices can harness in experiment.

2, The ability of measuring spectral phases with our SPIDER system is also restrained to seven Raman components. That is, even though we have a chance to improve the original powers of Raman generation, we have to seek new ways to measure spectral phases of eight or more Raman components. Refer to the former discussion.

Brief discussions of stability in amplitude and phase manipulations

The stability in both MA and MP is fine, due to a few reasons. First, the stages themselves are stable, precise, and reproductive; and materials in MA and MP are installed on such stages with a tiny slit separating each pair. Such a set itself is stable. Second, although there is no special facility for making the temperature in materials of MA and MP a constant, optical elements in

both MA and MP are transparent for such a broad spectrum, and hence heat via transmitting materials is negligible. Third, although we are manipulating amplitudes and phases with materials translating at a resolution of micrometers; however, whatever in MA or MP, translating such a scale by fluctuation of temperature is impossible.

5.3 Discussions in reconstructing electric field intensity waveforms

What are the differences between reconstructed electric field intensity waveforms of five, six, and seven Raman components?

According to Fourier transformation, pulse duration (at FWHM) depends on the distributions of amplitudes and phases, and also the bandwidth of spectrum. The former two factors have been discussed in the above two sections. As for the last factor, the broader the bandwidth is in the frequency domain, the narrower the pulse duration is in the time domain.

Comparing figures 4.10, 4.11, and 4.12, pulses remain in similar shapes with flanks suppressed.

Following escalation of the number of Raman components, pulse width decreases from 1.6 fs (five) to 1.4 fs (six), and ultimately to 1.2 fs (seven).

How much difference of pulse width is due to slight change of power distribution between MA and MP?

Since the experiments of MA and MP were basically on different dates, the power distributions were slightly different in front of SPIDER-DS system, causing nuanced change to the pulse width. Table 5.6 shows such difference.

Item	Five RCs		Six RCs		Seven RCs	
Type	Power of MA (kW)	Power of MP (kW)	Power of MA (kW)	Power of MP (kW)	Power of MA (kW)	Power of MP (kW)
2,403 nm	7.43	6.14	3.74	2.86	8.71	2.71
1,202 nm	13.71	19.57	18.86	20.57	4.14	17.14
801 nm	12.86	25.71	17.29	25.00	16.29	24.43
601 nm	14.71	8.57	11.29	9.57	27.29	16.57
481 nm	3.29	7.43	9.43	7.43	9.00	4.43
400 nm			7.29	5.43	13.57	9.14
343 nm					5.43	2.00
Pulse width (fs)	1.6111	1.6353	1.3198	1.3834	1.1320	1.2180
Difference (fs)	0.0242		0.0636		0.086	

Table 5.6: Difference of pulse width due to change of power distributions between MA and MP.

How much is the peak of adjacent cycle comparing to normalized global-maximum?

In optical communications, people are concerned about the ratio of normalized global maximum to the peak of adjacent cycle regarding ultrashort pulses.

The normalized global maximum of the pulses is 0.998 for five RCs. The peak of two flanks (adjacent cycle) next to the global maximum is 0.029. The ratio of global maximum to peak of adjacent cycle is 34.41 (or 15.33 dB). Similarly, global maximum, peak of adjacent cycle, and ratio of global maximum to peak of adjacent cycle are: 0.996, 0.052, and 19.15 (or 12.82 dB) for six RCs; 0.988, 0.072, and 13.68 (or 11.36 dB) for seven RCs.

For ultrashort pulses achieved at optimal point, we can see that these "ratios" for different number of Raman components maintain rather high values, which is preferable in optical communications.

What is next for narrowing down pulse width?

By far, we have achieved a series of ultrafast pulse trains, with the narrowest width (at FWHM) being 1.2 fs. However, we expect to further shorten pulse width to sub-1 fs, namely, about attosecond level.

We have assessed that with seven Raman components handled, under current situation (low power of generated Raman components–2,403 nm and 343 nm), it is almost impossible to achieve attosecond pulses by deeply manipulating amplitudes of them. Even though we find a way to enhance Raman generation and improve the powers of 2,403 nm and 343 nm, we may not tailor the amplitudes of seven RCs well within limited translation range of CQ thickness in MA. However, if we can find a suitable way to measure the phases of eight Raman components (refer to above discussions of the restraint of SPIDER-DS system), we can reconstruct a train of attosecond pulses. Refer to figure 4.13.

Bibliography of Chapter 5

[89] G. Ghosh. “Dispersion-equation coefficients for the refractive index and birefringence of calcite and quartz crystals”. In: *Opt. Comm.* 163 (1999), pp. 95–102.

[90] B.C. Stuart et al. “Laser-induced damage in dielectrics with nanosecond to subpicosecond pulses”. In: *Phys. Rev. Lett.* 74 (1995), pp. 2249–2251.

Chapter 6

Conclusions and prospects

6.1 Conclusions

In conclusion, I have proposed and experimentally demonstrated a novel optical technology, which allows us to arbitrarily manipulate amplitudes and phases of highly discrete broadband spectra.

The optical technology itself is simple–we just place a pair of wedge-shaped crystal quartz with a Glan laser polarizer, and two pairs of fused silica and calcium fluoride respectively on an optical axis, and precisely control their thicknesses.

As solid evidence of the reliability of our optical technology, we have manipulated the amplitudes and phases of five, six, and seven coherent vibrational Raman components in sequence, which have a frequency spacing of about 125 THz, and covers wavelength regions of mid-infrared, visible, and ultraviolet.

For both amplitude and phase manipulations, as the number of Raman components rises, the difficulty of arbitrary manipulations also increases. To be specific, for amplitude manipulation with more Raman components, we have to extend the range of numerical exploration for the optimum. For phase manipulation with more Raman components, we have to increase experimental resolution of intensity 'mapping' for the optimum.

As a typical application of the novel optical technology, we have also reconstructed electric field intensity waveforms in the time domain, based on achieved results of MA and MP. With five Raman components (2,403–481 nm) handled, we have achieved a train of 1.6 fs ultrafast pulses with a repetition period of 8.02 fs, near TL condition. With six Raman components (2,403–400 nm), we have achieved a train of 1.4 fs ultrafast pulses near TL condition. And with seven Raman components (2,403–343 nm), we have achieved a train of 1.2 fs ultrafast pulses near TL condition. This is the current situation of ultrafast pulses we have produced using the devices of MA and MP.

Additionally, a prominent feature of this optical technology is that the manipulations are performed on a coaxial optical path without separating broad spectra in space. As imagined from recent intensive studies regarding coherent combining technology, such arbitrary amplitude/ phase manipulation on a coaxial optical path should be very advantageous for practically maintaining high beam quality and mutual coherence in time and space among broad spectra. Also this technology is scalable to a high power laser, or a micro-scale system.

6.2 Prospects

Using our manipulation devices for controlling amplitudes and phases, we expect to broaden the bandwidth to handle eight or more high-order Raman components.

However, the most difficult issue of handling eight or more Raman components comes to measuring their spectral phases, which is beyond the capability of current SPIDER-DS system. Consequently, we have to seek an appropriate way to tackle such problem. If technically allowed to fabricate 5 μm thick BBO crystals, the above problem can be solved by substituting the 10 μm thick BBO in the current SPIDER-DS system.

Other labmates [91] have reported the possibility of using our novel optical technology, especially phase manipulation, to produce lasers in the vacuum

ultraviolet (VUV) region. Hence, we expect that our novel optical technology can be applied to generate VUV lasers in experiment.

Recent years, F. Krausz and his collaborators reported that the optical-field-induced electric currents in dielectrics can be driven, directed and switched by the instantaneous light field (bandwidth in petahertz domain); D. Brida and his collaborators reported to control electronic transport in a nanoantenna by varying the carrier-envelope phases of 6-fs-long pulses and demonstrated a robust class of nanoelectronic switches. Our optical technology and its achievement, generation of ultrashort pulses with ultrahigh-repetition-period (about eight femtoseconds), may become one of key tools for light-to-light ultrafast information processing [63–65].

Bibliography of Chapter 6

[91] J. Zheng and M. Katsuragawa. “Freely designable optical frequency conversion in Raman-resonant four-wave-mixing process”. In: *Sci. Reports* 5 (2015), p. 8874.

Appendix A

Comprehensive scales of manipulation devices

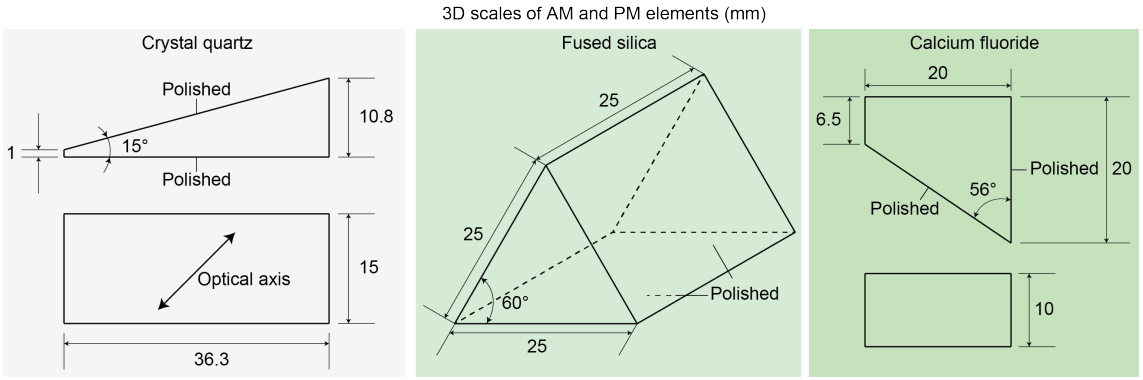

Figure A1: Comprehensive scales of manipulation devices.

Figure A1 shows 3D scales of optical elements in MA and MP devices. See also figure 3.4 for their shapes and placing methods.

To be specific, optical elements of MA are wedge-shaped crystal quartz, whose top view is triangular. The right-angled surface has an apex angle of 15 degrees with respect to the minimal side length of 10.8 mm. The wedges have a top height of 15 mm.

The optical elements of MP are made of two kinds of materials: fused silica and calcite fluoride. In detail, fused silica, whose top view is an equilateral triangle (side length: 25 mm), have a vertical height of 25 mm. The top view of calcite fluoride is trapezoidal, with a vertical height of 10 mm and an apex of 56 degrees.

Publications

Papers

- **Chuan Zhang**, Kazumichi Yoshii, Dmitry Tregubov, Chiaki Ohae, Jian Zheng, Masaru Suzuki, Kaoru Minoshima, and Masayuki Katsuragawa, "Optical technology for arbitrarily manipulating amplitudes and phases of coaxially propagating highly discrete spectra," Phys. Rev. A **100,** 053836 (2019).

Proceedings

- **Chuan Zhang**, Kazumichi Yoshii, Dmitry Tregubov, Chiaki Ohae, Masaru Suzuki, Kaoru Minoshima, and Masayuki Katsuragawa, "Generation of 1.4-fs ultrafast single-cycle pulses with a repetition rate exceeding 100 THz by arbitrarily manipulating amplitude and phase," CLEO 2018, San Jose, USA (2018).

Conference contributions-international

- **Chuan Zhang**, Dmitry Tregubov, Kazumichi Yoshii, Chiaki Ohae, Masaru Suzuki, Kaoru Minoshima, and Masayuki Katsuragawa, "Simple optical technology to arbitrarily manipulate amplitude and phase and its application to generation of ultrafast pulses above 100 THz repetition rate," ICO-24, Tokyo, Japan (2017) [*Oral*].

- Masayuki Katsuragawa, Chiaki Ohae, Jian Zheng, **Chuan Zhang**, Trivikramarao Gavara, Masaru Suzuki, and Kaoru Minoshima, "Tailored optics with a highly-discrete optical frequency comb," ICO-24, Tokyo, Japan (2017) [*Oral*].

- **Chuan Zhang**, Dmitry Tregubov, Kazumichi Yoshii, Chiaki Ohae, Masaru Suzuki, Kaoru Minoshima, and Masayuki Katsuragawa, "A new optical technology to arbitrarily manipulate amplitudes and phases of a highly discrete broadband spectrum," MIPT-UEC Workshop, Tokyo, Japan (2017) [*Poster*].

- **Chuan Zhang**, Kazumichi Yoshii, and Masayuki Katsuragawa, "Generation of 1.8 fs pulse train by simply controlling thicknesses of transparent-plates placed on the optical path," MIPT-UEC Workshop, Moscow, Russia (2015) [*Oral* & *Poster*].

Conference contributions-domestic

- **Chuan Zhang**, Dmitry Tregubov, Kazumichi Yoshii, Chiaki Ohae, Masaru Suzuki, Kaoru Minoshima, and Masayuki Katsuragawa, "A new optical technology of arbitrarily manipulating amplitudes and phases of a highly-discrete broad spectrum," JSAP, Fukuoka, Japan (2017) [*Oral*].
- **Chuan Zhang**, Dmitry Tregubov, Kazumichi Yoshii, Chiaki Ohae, Masaru Suzuki, Kaoru Minoshima, and Masayuki Katsuragawa, "A simple means of arbitrarily manipulating amplitudes and phases of broadband optical waves and its application to generation of ultrashort pulses," Laser Society of Japan, Tokushima, Japan (2017) [*Oral*].
- **Chuan Zhang**, Dmitry Tregubov, Kazumichi Yoshii, Chiaki Ohae, Masaru Suzuki, Kaoru Minoshima, and Masayuki Katsuragawa, "Arbitrary manipulation of amplitudes and phases of broadband optical waves and its application to generation of ultrashort pulses," JSAP, Niigata, Japan (2016) [*Oral*].

Awards

- *Award for Excellent Research Work*
  The University of Electro-Communications, Tokyo, Japan (2018).

- *OSA/SPIE Student Paper Award at ICO-24*
  Chuan Zhang, Dmitry Tregubov, Kazumichi Yoshii, Chiaki Ohae, Masaru Suzuki, Kaoru Minoshima, and Masayuki Katsuragawa, "Simple optical technology to arbitrarily manipulate amplitude and phase and its application to generation of ultrafast pulses above 100 THz repetition rate," ICO-24, Tokyo, Japan (2017).

- *Award for Excellent Paper Presentation*
  Chuan Zhang, Dmitry Tregubov, Kazumichi Yoshii, Chiaki Ohae, Masaru Suzuki, Kaoru Minoshima, and Masayuki Katsuragawa, "A simple means of arbitrarily manipulating amplitudes and phases of broadband optical waves and its application to generation of ultrashort pulses," Laser Society of Japan, Tokushima, Japan (2017).